



THE UNIVERSITY *of* EDINBURGH

Edinburgh Research Explorer

VHMS mineralisation at Erayinia in the Eastern Goldfields Superterrane

Citation for published version:

Hollis, SP, Podmore, D, James, M, Menuge, JF, Doran, AL, Yeats, CJ & Wyche, S 2019, 'VHMS mineralisation at Erayinia in the Eastern Goldfields Superterrane: Geology and geochemistry of the metamorphosed King Zn deposit', *Australian journal of earth sciences*, vol. 66, no. 2, pp. 153-181. <https://doi.org/10.1080/08120099.2018.1515577>

Digital Object Identifier (DOI):

[10.1080/08120099.2018.1515577](https://doi.org/10.1080/08120099.2018.1515577)

Link:

[Link to publication record in Edinburgh Research Explorer](#)

Document Version:

Peer reviewed version

Published In:

Australian journal of earth sciences

General rights

Copyright for the publications made accessible via the Edinburgh Research Explorer is retained by the author(s) and / or other copyright owners and it is a condition of accessing these publications that users recognise and abide by the legal requirements associated with these rights.

Take down policy

The University of Edinburgh has made every reasonable effort to ensure that Edinburgh Research Explorer content complies with UK legislation. If you believe that the public display of this file breaches copyright please contact openaccess@ed.ac.uk providing details, and we will remove access to the work immediately and investigate your claim.



1 VHMS mineralization at Erayinia in the Eastern Goldfields
2 Superterrane: Geology and geochemistry of the metamorphosed King
3 Zn deposit

4
5 Steven P. Hollis^{1,2,3*}, Darryl Podmore⁴, Megan James⁴, Julian F. Menuge¹, Aileen L.
6 Doran¹, Christopher J. Yeats^{2,5} & Stephen Wyche³

7
8 ¹iCRAG (Irish Centre for Research in Applied Geosciences) and School of Earth Sciences, University
9 College Dublin, Belfield, Dublin 4, Ireland *E-mail: steve.hollis@icrag-centre.org

10 ²CSIRO Earth Science and Resource Engineering, 26 Dick Perry Avenue, Kensington, Western
11 Australia, 6151, Australia

12 ³Geological Survey Division, Department of Mines and Petroleum, East Perth, Western Australia, 6004,
13 Australia

14 ⁴Black Raven Mining, PO Box 902, West Perth, Western Australia, 6872, Australia

15 ⁵Geological Survey of New South Wales, NSW Department of Industry, 516 High St, Maitland, New
16 South Wales, 2320, Australia

17
18 A manuscript for *Australian Journal of Earth Sciences*

19 Keywords: volcanic-hosted massive sulfide; Archaean; Yilgarn Craton; litho-geochemistry;
20 pXRF.

21
22 **Abstract**

23 Despite having been a target for volcanic-hosted massive sulfide (VHMS) deposits
24 since the 1960s, few resources have been defined in the Archean Yilgarn Craton of Western
25 Australia. Exploration challenges associated with regolith and deep cover exacerbate the
26 already difficult task of exploring for small, deformed deposits in stratigraphically complex,
27 metamorphosed volcanic terranes. We present results of drillcore logging, petrography, whole
28 rock geochemistry and pXRF data from the King Zn deposit, to help refine mineralogical and
29 geochemical halos associated with VHMS mineralization in amphibolite facies greenstone
30 sequences of the Yilgarn Craton.

31 The King Zn deposit (2.15 Mt at 3.47% Zn) occurs as a 2-5m thick stratiform lens
32 dominated by iron sulfides, in an overturned, metamorphosed volcanic rock-dominated
33 sequence located ~140km east of Kalgoorlie. The local stratigraphy is characterized by garnet
34 amphibolite and strongly banded intermediate to felsic schists, with rare horizons of graphitic
35 schist. Massive sulfide mineralization is characterized by stratiform pyrite–pyrrhotite–
36 sphalerite at the contact between quartz-muscovite schists (‘the footwall dacite’) and banded
37 quartz-biotite/amphibole±garnet schists of the stratigraphic hanging-wall. A zone of pyrite-
38 (sphalerite) and pyrrhotite–pyrite–(chalcopyrite) veining extends throughout the stratigraphic
39 footwall. Footwall garnet-amphibolites are of sub-alkaline basaltic affinity, with a central zone
40 dominated by chlorite±magnetite interpreted to represent the Cu-bearing feeder zone. SiO₂,
41 CaO, Fe₂O_{3T}, MgO and Cu concentrations are highly variable, reflecting quartz–
42 epidote±chlorite±magnetite±sulfide alteration. Hydrothermal alteration in stratigraphically
43 overlying intermediate to felsic rocks is characterized by a mineral assemblage of quartz–

44 muscovite±chlorite±albite±carbonate. Cordierite and anthophyllite are locally significant and
45 indicative of zones of Mg-metasomatism prior to metamorphism. Increases of SiO₂, Fe₂O_{3T},
46 pathfinder elements (e.g. As, Sb, Tl), and depletions of Na₂O, CaO, Sr, and MgO occur in
47 footwall quartz-muscovite schists approaching massive sulfide mineralization.

48 Within all strata (including the immediate hanging-wall), the following pathfinder
49 elements are strongly correlated with Zn: Ag, As, Au, Bi, Cd, Eu/Eu*, Hg, In, Ni, Pb, Sb, Se,
50 Tl. These geochemical halos resemble less metamorphosed VHMS deposits across the Yilgarn
51 Craton and suggest that although metamorphism leads to element mobility and mineral
52 segregation at the thin section scale, assay samples of ~20cm length are sufficient to vector to
53 mineralization in amphibolite facies greenstone belts. Recognition of minerals such as Mg-
54 chlorite, muscovite, cordierite, anthophyllite, biotite/phlogopite, and abundant garnet are
55 significant, in addition to Al-rich phases (i.e. kyanite, sillimanite, andalusite and/or staurolite)
56 not identified at King. Chemographic diagrams may be used to identify and distinguish
57 different alteration trends, along with several alteration indices (e.g. AI, CCPI, SI) and the
58 abundance of normative corundum and quartz.

59

60 1. Introduction

61 For the last four decades, exploration for volcanic-hosted massive sulfide (VHMS)
62 mineralization in the Archean Yilgarn Craton of Western Australia (**Fig. 1**) has been hampered
63 by a perceived lack of prospectivity and difficult exploration conditions. The latter include
64 deep and transported overburden, a paucity of outcrop, high strain, and saline groundwaters
65 (McConachy et al. 2004; Yeats, 2007; Vearncombe, 2010; Hollis et al. 2015). In many
66 greenstone belts, the proximity of supracrustal rocks to late stage granites, which comprise
67 much of the craton, adds further complications. Metamorphic grade varies across the craton
68 from greenschist to granulite facies, generally being higher closer to greenstone margins, and
69 within narrower greenstone belts (e.g. Witt, 1991; Swager, 1997; Witt & Hagemann, 2012).

70 Few VHMS deposits have been identified in greenstone sequences metamorphosed to
71 relatively high grade in the Yilgarn Craton (reviewed in Hollis et al. 2017a), as relatively simple
72 primary alteration assemblages are often overprinted and obscured, with host rocks now
73 comprising mineralogically complex banded schist or gneiss. For example, at Kingsley (the
74 Wheatley prospect, South West Terrane: **Fig. 1**), massive sulfide mineralization is hosted at a
75 transition between quartz-feldspar-biotite gneiss and hornblende-plagioclase-biotite-
76 quartz±garnet amphibolite, marking a shift from felsic to mafic volcanism (Yeats, 2007;
77 Hassan, 2017a). Sodium depletion in felsic gneisses underneath mineralization and the Al-rich
78 minerals sillimanite, staurolite, kyanite and garnet provide evidence for a metamorphosed
79 hydrothermal system (Yeats, 2007; Hassan, 2017a). In the eastern half of the Quinns district
80 (Murchison Domain, Youanmi Terrane: **Fig. 1**), schistose rhyolite contains locally abundant
81 and coarse-grained andalusite±kyanite±garnet where associated with VHMS mineralization
82 (Duuring et al. 2016; Hassan, 2017b). The recognition of garnet and staurolite porphyroblasts
83 for 30m above and below the Hollandaire deposit (Murchison Domain, Youanmi Terrane: **Fig.**
84 **1**) was also significant for VHMS exploration in the area (Hayman et al. 2015a).

85 Despite the increased difficulty of discovery, the metamorphism and deformation of
86 VHMS deposits may bring economic benefits. These can include the significant upgrading and

87 redistribution of gold during metamorphism (e.g. Boliden deposit, Sweden; [Wagner, et al.](#)
88 [2007](#)), and the thickening of massive sulfide ores in hinge zones of folds ([Dusel-Bacon, 2012](#)).
89 We present results of drillcore logging, petrography, whole rock geochemistry and pXRF data
90 from the King Zn VHMS deposit in the Erayinia region of the southern Kurnalpi Terrane
91 (Edjudina Domain, **Fig. 1**). We show that the mineralogical and geochemical signatures of the
92 magmatic, hydrothermal and metamorphic events can be resolved. From these inferences we
93 discuss features that may be used to identify VHMS deposits that have been metamorphosed
94 at amphibolite facies in the Yilgarn Craton.

95

96 **2. Geological setting**

97 The Yilgarn Craton has historically been divided into a series of terranes based on distinct
98 lithological associations, geochemistry and ages of volcanism ([Gee et al. 1981](#); [Myers, 1990](#);
99 [Cassidy et al. 2006](#)). The western half of the Yilgarn Craton comprises the Narryer, South West
100 and Youanmi terranes (**Fig. 1**). East of the Ida Fault, the Eastern Goldfields Superterrane (EGS)
101 can be divided into the Kalgoorlie, Kurnalpi, Burtville and Yamarna terranes ([Pawley et al.](#)
102 [2012](#); **Fig. 1**). The geology of the Yilgarn Craton with respect to VHMS mineralization has
103 recently been discussed by [Hollis et al. \(2015; 2017a\)](#). Here we summarise the regional geology
104 of the Kalgoorlie and Kurnalpi terranes (**Figs. 1 & 2**).

105 The geology of the Kalgoorlie Terrane is broadly divisible into the lower 2720-2690
106 Ma mafic-ultramafic Kambalda Sequence ([Beresford et al. 2005](#)) and the overlying 2690-2660
107 Ma Kalgoorlie Sequence ([Krapež & Hand, 2008](#)) (**Fig. 2**). At least two magmatic cycles,
108 interpreted as plume related, are recognized in the lower sequence ([Hayman et al. 2015b](#)). The
109 overlying 2690-2660 Ma Kalgoorlie Sequence comprises a >3km thick package of
110 volcanoclastic rocks, felsic volcanic rocks, and mafic intrusive complexes with minor mafic
111 volcanic rocks ([Squire et al. 2010](#); **Fig. 2**). Late doming and extension associated with the
112 emplacement of a widespread tonalite-trondjemite-granodiorite (TTG) suite produced the late
113 clastic basins of the Eastern Goldfields ([Wyche et al. 2013](#); **Fig. 2**).

114 Broadly coeval with the Kambalda Sequence of the Kalgoorlie Terrane, the Kurnalpi
115 and Minerie sequences of the Kurnalpi Terrane are represented by a more intermediate package
116 of rocks (**Fig. 2**). Although some workers have attributed the Kurnalpi andesites to an Archaean
117 arc (and thus the Kalgoorlie Terrane to a back-arc; e.g. [Czarnota et al. 2010](#)), they are also
118 geochemically consistent with the fractionation of plume-related tholeiitic basalts, coupled
119 with their contamination by contemporaneous partial melts of pre-existing continental crust
120 ([Barnes & Van Kranendonk, 2014](#)). Between 2692 and 2680 Ma, volcanic centres in the
121 Kurnalpi Terrane (Gindalbie Domain and further south; **Fig. 1**) are associated with largely
122 bimodal (basalt-rhyolite) volcanic and associated sedimentary rocks, although some contain
123 significant volumes of andesites (**Fig. 2**). These felsic rocks are significantly enriched in the
124 high field strength elements (HFSE) and heavy rare earth elements (HREE) ([Brown et al. 2002](#);
125 [Barley et al. 2008](#); [Hollis et al. 2015](#)), and are diagnostic of shallow crustal melting ([Leshner et al.](#)
126 [1986](#); [Piercey et al. 2001](#); [Hart et al. 2004](#)). This region of HFSE-enriched felsic volcanic
127 rocks and broadly coeval HFSE-enriched granitic intrusions ([Hollis et al. 2015](#)) coincides with
128 an area of juvenile crust revealed through regional Sm-Nd (granite; **Fig. 3**) and Pb isotope

129 (galena) variations (Huston et al. 2005, 2014). Interpreted as a paleo-rift zone, where juvenile
130 material was added to the crust, similar isotopic features have also been recognized in the
131 Youanmi Terrane (i.e. Cue Zone) and Abitibi-Wawa subprovince of Canada where they are
132 associated with VHMS mineralization (Huston et al. 2014). To date only three VHMS deposits
133 have been mined in the Eastern Goldfields Superterrane - all from the c. 2690 Ma Teutonic
134 Bore volcanic complex (Hallberg & Thompson, 1985; Belford et al. 2015; Fig. 3). A significant
135 resource of Ag-rich VHMS mineralization has also been recognized in the Kalgoorlie Terrane
136 at Nimbus (Fig. 3), interpreted to represent a shallow water and low temperature deposit
137 formed on the margin of the Kurnalpi rift zone at c. 2705 Ma (Hollis et al. 2017b).

138 3. Regional Geology of Erayinia

139 The regional geology of the Erayinia area in the southern Kurnalpi Terrane is detailed
140 in the 1:100,000 GSWA explanatory notes (Jones, 2007). Two major faults (Claypan and Roe
141 Hills) divide the area into three domains - Edjudina, Murrin and Menangina (Fig. 4). As the
142 Edjudina Domain at King is the focus of this paper, the other two domains will not be discussed.
143 An account of VHMS mineralization in the Murrin Domain ~4km NW of King will be
144 presented elsewhere (Hollis et al. in prep).

145 The Edjudina Domain across its ~300km length (Fig. 1) is dominated by several
146 basaltic to rhyolitic volcanic complexes, and laterally extensive belts of intermediate schist
147 predominantly derived from andesitic precursors (Swager, 1995, 1997). Prominent, though
148 volumetrically minor, marker beds of banded iron formations (BIF), chert and fine grained
149 metasedimentary rocks cap the aforementioned sequence, which are intruded by extensive
150 dolerite sills (Swager, 1995, 1997). A narrow eastern belt of thin basalt which contains
151 komatiite layers was also recognized. Existing U-Pb zircon ages from the southern half of the
152 Edjudina Domain are limited to: i) 2708 ± 6 Ma from a fragmental metadacite porphyry in a
153 felsic sequence associated with calc-alkaline rocks ~100km N of King (Nelson, 1995); ii) 2698
154 ± 10 Ma from a metatonalite intrusion also ~100km N of King (Nelson, 1996); and iii) $2680 \pm$
155 4 Ma from a granite gneiss at Coonana Hill ~30km NE of King (Wingate et al. 2016). The
156 distribution of komatiite and BIF within the southern Eastern Goldfields, along with all current
157 U-Pb zircon ages from the region, is shown in Figure 5.

158 Jones (2007) provides a more local summary of the geology at Erayinia east of the
159 Claypan Fault (Fig. 4). According to Jones (2007), greenstone sequences contain interlayered
160 mafic and felsic schists, ferruginous chert bands and silicified black shales that define tight
161 folds on aeromagnetic images. Further east, along the eastern margin of Erayinia, thin units of
162 meta-ultramafic rocks (komatiite?) and metabasalt are interlayered with metasedimentary
163 rocks (Fig. 4). The mapped meta-ultramafic rocks are preserved as deeply weathered talc-
164 chlorite-(carbonate) schists ~17 SE of King (Fig. 4) (Jones, 2007). Together with the presence
165 of a large rubbly outcrop of Fe-rich chert ~10km N of King, that is similar in appearance to
166 BIF (Jones, 2007), this may suggest the local stratigraphy is >2.7 Ga in age and belongs to the
167 Minerie or Kurnalpi sequence (Fig. 2). The Gindalbie age (2680 ± 4 Ma) from a 'granite gneiss'
168 at Coonana Hill ~30km NE of King (Wingate et al. 2006; Fig. 5) may belong to a similar
169 sequence to the 'schist derived from granite rock' mapped by Jones (2007) in Figure 4.

170 Unfortunately, our attempted U-Pb dating of the King stratigraphy was unsuccessful due to a
171 paucity of zircons recovered from footwall quartz-muscovite schists.

172 Regional deformation of the Erayinia region is complex and typically involved an early
173 extensional event (D_E), followed by: D_1 compression involving thrusting and recumbent
174 folding (F_1); D_2 ENE-WSW crustal shortening, producing major upright folding (F_2 : 2675-
175 2657 Ma); D_3 sinistral movement and associated folding on NNW-trending regional strike slip
176 faults; and D_4 overprinting with oblique reverse movements on the same structures (Jones,
177 2007).

178 Peak metamorphism across the Eastern Goldfields is most intense (upper amphibolite
179 facies) surrounding large granitoid bodies that were emplaced at 2660-2640 Ma, broadly
180 contemporaneous with D_2 deformation (Witt, 1991; Nelson, 1997; Swager et al. 1997). Away
181 from these granitoids, porphyroblasts of biotite and andalusite grew over and across the vertical
182 regional foliation indicating the relatively late timing of peak regional metamorphic conditions
183 (Swager, 1997). Lower grade zones of greenschist facies metamorphism are found in the
184 central parts of greenstone belts (Jones, 2007). A marked increase in metamorphic grade was
185 noted by Jones (2007) across the Claypan Fault (Fig. 4), from relatively undeformed
186 greenschist facies felsic volcanoclastic rocks and basalt in the west, to muscovite schist,
187 chlorite-muscovite schist, and biotite-garnet schist east of the fault.

188 4. King deposit stratigraphy

189 The King Zn deposit (~2.146 Mt at 3.47% Zn, non-compliant at 1% cut off) occurs in an
190 overturned and east-dipping volcanic-dominated sequence (Fig. 6) located approximately
191 140km east of Kalgoorlie (Fig. 1) and 36km south of the Trans Australian Railway. Although
192 the area had previously been explored for uranium and gold, base-metal mineralization was
193 first targeted during the 1990s by Sons of Gwalia. Following geological mapping, ground
194 magnetometry and surface TEM geophysics, a conductor was recognized as coincident with a
195 magnetic anomaly. Further soil sampling and Reverse Circulation (RC) drilling led to the
196 interception of narrow massive sulfide layers at King (formerly called Calliope). The most
197 extensive exploration activity was undertaken by ABM Resources from 2005 to 2012 as the
198 manager of a joint venture with Hawthorn Resources Ltd (detailed in Podmore & James, 2016).
199 Subsequent diamond, RC and Rotary Air Blast (RAB) drilling by ABM defined the current
200 size of the King deposit (Figs. 6a, b). More recently, a soil and rock chip sampling programme,
201 and VTEM (Versatile Time Domain EM) geophysical survey, was undertaken by Black Raven
202 Mining (2012-2017) over the extended licence areas.

203 Our current interpretation is that the volcanic stratigraphy at King is overturned and
204 dipping to the east (Fig. 6c). This is based on metal zonation in the deposit, and the distribution
205 and intensity of logged hydrothermal alteration assemblages (see Discussion). An intensely
206 chloritized zone of discordant alteration with abundant chalcopyrite and Fe-sulfides lies above
207 a sheet-like body of massive Fe-Zn sulfide (Fig. 6d), the opposite to most VHMS systems
208 (Hannington et al. 2005; Galley et al. 2007). Graded were beds also noted by ABM geologists
209 from drillholes EC120D and EC116D (ABM Resources NL, 2008) consistent with our

210 interpretation, although these have not been verified since. Possible graded bedding from hole
211 EC056D is shown in **Figure 7I**. An overturned stratigraphy is also consistent with Swager's
212 (1995, 1997) description of rocks from the Edjudina domain - namely basaltic to felsic volcanic
213 complexes, overlain by fine grained sedimentary rocks, chert and BIF intruded by mafic sills
214 – and also a recent study from King North (Kelly, 2018, unpublished thesis; **Fig. 4**).

215 Photographs of the main lithologies and styles of mineralization present in diamond
216 drillcore are shown in **Figures 7 and 8**. The stratigraphy at the King deposit from interpreted
217 stratigraphic footwall to hanging-wall, assuming an overturned stratigraphy (**Fig. 6c**), is
218 characterised by:

219 **Footwall garnet-amphibolite:** A thick (>300m) sequence of foliated garnet-amphibolite or
220 hornblende-garnet-quartz schist (**Figs. 7ab, 9a**) occurs in the deep stratigraphic footwall of the
221 King deposit, with the top contact now ~100-150m above mineralization (**Fig. 6c**). The
222 groundmass is dominated by fine granulose green hornblende with interstitial fine anhedral
223 quartz, minor epidote, and carbonate (**Fig. 9a**). Garnet porphyroblasts contain quartz and
224 hornblende inclusions. A general anastomosing schistosity (**Fig. 7b**) is paralleled by the
225 granulose hornblende texture. Local zones with abundant ragged and acicular actinolite (to
226 ~3mm in drillcore) also occur. Towards the centre of the King deposit a zone characterized by
227 abundant chlorite is present (**Figs. 6d, 9d**). This is best observed in drillhole EC116D where
228 fine magnetite crystals are disseminated throughout the core in close association with
229 chalcopyrite±pyrite blebs and stringers (**Figs. 8a-b, 9b-c**). Contacts are gradational with
230 surrounding garnet-amphibolites, with the change in rock type reflecting an increased
231 abundance of chlorite±magnetite to hornblende-garnet-quartz.

232 The thick sequence garnet-amphibolite is interpreted to represent a sheared and
233 metamorphosed sequence of mafic rocks. It is unclear due to the strong banding and
234 recrystallization whether these represent metamorphosed coherent mafic flows, volcanoclastic
235 rocks or thick basaltic sills. Primary volcanic textures such as pillows, varioles, chilled margins
236 and peperite are not preserved. Similar mafic lithologies have been mapped by Jones (2007)
237 along strike to the north of the King deposit (weakly foliated amphibolite; **Fig. 4**). Quartz and
238 epidote altered mafic volcanic rocks (greenschist facies) have also been recently drilled at King
239 North along strike (**Fig. 4**), which are geochemically similar to those described here (Kelly,
240 2018, unpublished thesis). The zone of intense chlorite with Cu-Fe sulfides is interpreted to
241 represent the feeder zone to massive sulfide mineralization that was enriched in Mg prior to
242 metamorphism (see Discussion).

243 **Mixed footwall sequence:** Stratigraphically overlying the garnet amphibolite is a ~30 to 130m
244 thick mixed sequence of intensely altered, intermediate to felsic schist. Rare units (<15m thick)
245 resembling the aforementioned footwall garnet-amphibolite also occur. Rocks of the mixed
246 footwall sequence are highly variable in their mineralogy and are strongly banded and folded
247 (**Figs. 7d-g**). More leucocratic (intermediate to felsic) lithologies are dominated by a
248 combination of quartz, chlorite and carbonate with lesser hornblende, biotite and epidote (**Figs.**
249 **9e-h**). Where present, biotite parallels the schistosity and is often retrogressed to chlorite.
250 Leucoxene, zircon and titanite are present as accessory phases. Zones rich in albite and/or

251 muscovite also occur. In the rare mafic lithologies, the metamorphic matrix is dominated by
252 hornblende with minor epidote in darker bands, and quartz-epidote-chlorite in paler bands.

253

254 Throughout each of the drillholes logged at the King deposit (**Fig. 6a**) a distinct zone
255 of intense brown and green banding is common (**Fig. 7d**). This occurs at depths anywhere from
256 ~50 to 150m in the footwall to massive sulfide mineralization and varies in thickness from a
257 few metres to tens of metres. This lithology is characterized by quartz, anthophyllite,
258 clinozoisite and biotite (intergrown with anthophyllite and replaced by chlorite) (**Fig. 9f-h**).

259

260 The mixed footwall sequence is interpreted to represent a package of metamorphosed
261 intermediate to felsic volcanoclastic rocks, with rare mafic sills/lava flows (now garnet-
262 amphibolite) and thin beds of deep marine argillaceous sediments (typically <2m thick;
263 preserved as graphitic schist; see section below). Rare examples of lapilli tuff have been
264 described from this sequence, with relict quartz clasts apparent in thin section. The zone rich
265 in anthophyllite is interpreted to reflect Mg-metasomatism prior to metamorphism in the
266 intermediate to felsic lithologies.

267

268 **Quartz-muscovite schist (footwall dacite):** A ~50 to 90m thick sequence of leucocratic and
269 variably banded quartz-muscovite schist of dacitic composition comprises the immediate
270 stratigraphic footwall to massive sulfide mineralization at King (**Figs. 6c, 7h**). In some
271 instances, coherent and weakly altered units occur in close proximity to mineralization,
272 surrounded by intensely altered and sheared lithologies. Quartz-muscovite schists are
273 dominated by fine granoblastic quartz with interstitial platy muscovite defining the schistosity
274 (**Figs. 9i-j**), and minor epidote. Locally, Mg-rich cordierite can be significant ($\leq 5\%$) as
275 aggregates and crystals throughout the matrix. This is often replaced by sericite and associated
276 Mg-chlorite. Bands of sericitised plagioclase occur in the matrix of some samples. Sulfides,
277 tourmaline, hornblende, leucoxene and zircon are present as accessory phases (**Fig. 9k**).
278 Garnets are rare, but small (<2mm) pink to red porphyroblasts are disseminated throughout
279 most units logged. Directly under massive sulfides (**Fig. 9l**, described in **Section 5**), the quartz-
280 muscovite schists are intensely silicified in hand specimen. With depth, an increase in
281 muscovite, chlorite and albite is clear in drillcore (**Fig. 6c**). Contacts between different styles
282 of alteration are gradational. Where present, pyrite and sphalerite occur as stringers and
283 disseminated throughout the host stratigraphy (**Figs. 8c, 9k**; see **Section 5**).

284

285 The thick sequence of quartz-muscovite schist is interpreted to represent a mixed,
286 hydrothermally altered and metamorphosed sequence of dacitic volcanoclastic rocks and more
287 coherent volcanic lithologies (either representing flows or high-level intrusions). No quartz or
288 feldspar phenocrysts were observed; all rocks examined in thin section are strongly
289 recrystallized and show evidence of shearing.

290

291 **Mixed hanging-wall sequence:** The immediate hanging-wall of the King deposit is dominated
292 by finely banded (mm to cm scale) schists of mafic to felsic composition (**Fig. 7i**), grouped
293 together here as quartz-biotite/amphibole±garnet schists. Banding reflects the varying

294 abundance of fine to medium granoblastic quartz (with lesser biotite) to
295 tremolite/actinolite±garnet (**Figs. 9o-p**). Garnet can be retrogressed to fibrous chlorite
296 aggregates with quartz. Calcite is present throughout the matrix, as well as in veinlets and vugs
297 (**Figs. 9q-r**). Magnetite is disseminated (3-5%) throughout the matrix of the banded schists
298 directly overlying massive sulfides (**Fig. 6**). In the deeper sections of the deposit where
299 magnetite has not been replaced by secondary Fe-oxides, a very strong magnetic signature
300 persists for ~1 to 4m into the stratigraphic hanging-wall. This zone is typically more magnetic
301 than the pyrrhotite-magnetite-bearing chloritic feeder zone, but the intensity of both varies
302 significantly from hole to hole. Pyrite stringers are abundant close to massive sulfides and are
303 strongly recrystallized. These pyrite parallel and cut metamorphic banding at high angles (**Fig.**
304 **8f**). The most convincing example of grading, shown in **Fig. 7l**, is consistent with an
305 overturned stratigraphy.

306 Thin horizons of graphitic schist (described below), pyrite-bearing polymict volcanic
307 breccias (**Fig. 7k**), and rare, coherent carbonate-altered rocks of mafic composition (herein
308 termed the hanging-wall amphibolites) are also present in the stratigraphic hanging-wall to
309 mineralization. The hanging-wall amphibolites (~3m thick) are dominated by amphibole and
310 quartz, with carbonate alteration and relict clinopyroxene. Garnets can be present, but not in
311 every drillhole. Finely banded chert-like rocks were noted at ~385m depth in drillhole EC056D
312 (**Fig. 7j**). The polymict volcanic breccias (~382m in EC056D) are intensely brecciated, quartz
313 veined, contain clasts up to 4cm of surrounding lithologies (e.g. layered chert, banded schist,
314 amphibolite), and thin stringers of magnetite.

315 The mixed hanging-wall sequence is interpreted to represent a sequence of
316 metamorphosed interbedded volcanic/volcaniclastic rocks of varying composition, with
317 interbedded fine grained, deep marine sedimentary rocks. The hanging-wall amphibolites may
318 represent very thin lava flows or coeval basaltic sills (e.g. [Swager, 1997](#)).

319 **Horizons of graphitic schist:** Thin (0.4-2m) horizons of graphitic schist have been identified
320 throughout the King stratigraphy in both the interpreted footwall (ED086 303m) and hanging-
321 wall (ED143 ~505m) to massive sulfide mineralization. Similar lithologies were also noted as
322 deformed fragments within the massive sulfide zone of drillhole EC116D, where they are
323 intensely chloritized and in some sections appear to have been replaced by sulfides. The
324 horizons of graphitic schist are always intensely fractured, strongly sheared, and can be
325 intermittently banded with surrounding lithologies (e.g. garnet amphibolite, quartz-muscovite
326 schists). In most instances fault gouges are closely associated with the graphitic schists,
327 indicative of thrusting in the stratigraphy. The graphitic schists most likely represent
328 metamorphosed deep marine argillaceous sediments precipitated under anoxic conditions.

329
330 **Quartz-feldspar pyritic intrusive rocks:** The King stratigraphy has been intruded by at least
331 two generations of quartz-feldspar porphyry sills that broadly parallel bedding (**Fig. 6**). The
332 earlier set appears to be broadly coeval with the volcanic stratigraphy and are ~0.7 to 1.5m
333 thick with sharp margins (e.g. at 309m EC056D; 387m EC116D). They exhibit a similar
334 mineralogy (quartz-muscovite) to the footwall felsic rocks they intrude, contain disseminated

335 sulfides, and have a strong foliation which parallels surrounding strata (**Fig. 6c**, labelled 1; **Fig.**
336 **7m**).

337 A presumably younger set of thinner (5-30cm) quartz-feldspar phyric sills intrude the
338 hanging-wall to massive sulfide mineralization in hole EC056D (~363m; **Fig. 6c**, labelled 2).
339 This suite is less foliated (**Fig. 7n**) and resemble those of the Erayinia NW area closely
340 associated with late high-Ca granitoid intrusions of the eastern Murrin Domain (**Hollis et al. in**
341 **prep**). Sharp unchilled margins are orientated parallel to banding in surrounding schists.

342 **Late basaltic dykes:** Late basaltic dykes crosscut the stratigraphy and are undeformed. These
343 rocks are typically ~0.5 to 2.5m thick, coarsen to doleritic centres, and display chilled margins
344 and varioles (**Fig. 7o**). They most likely belong to the Palaeoproterozoic Widgiemooltha Dyke
345 Suite (**Fig. 6**). The suite is clearly visible in regional magnetics and intrudes the area in
346 predominantly E-W and NNE-SSW orientations (**Fig. 4**).

347 **5. Sulfide mineralization at King**

348 Sulfide mineralization at King occurs predominantly as a stratiform, ~1 to 7m thick,
349 sheet-like body of massive pyrite-pyrrhotite with subordinate sphalerite, at the contact between
350 intensely silicified dacite (footwall quartz-muscovite schist) and banded quartz-
351 biotite/amphibole±garnet schist (**Fig. 6c**). This zone of stratiform massive sulfide
352 mineralization dips at 45-70° eastwards, has a confirmed depth of at least 400m, and has been
353 drilled across a strike length of ~600m (**Fig. 6a**). Diamond drilling is restricted to the central
354 450m (**Fig. 6a**). Two small, high-grade lenses of Zn mineralization have been recognised
355 separated by a central zone (150-200m long) with lower Zn grades (**Fig. 6b**). The best intercept
356 is 5m at 10.6% Zn in drillhole EC116D. There has been sporadic analysis for gold in both
357 massive sulfides and the feeder zone. Significant intercepts include 5m at 0.6 g/t Au (hole
358 EC046D) and 5.9m at 0.3g/t Au (EC031D) (**Fig. 6b**). Stratigraphically underlying the
359 stratiform massive sulfides a zone of discordant vein and disseminated sulfides (from pyrite-
360 sphalerite to pyrrhotite-chalcopyrite-pyrite; **Fig. 8a-b**) extends throughout the underlying strata
361 (**Fig. 6d**). It is important to note that all sulfide assemblages show evidence for
362 recrystallization.

363 Within the massive sulfides two broad styles of mineralization can be defined: a lower
364 zone characterized by fine to coarse grained subhedral pyrite with replacive interstitial
365 red/brown sphalerite (**Fig. 8d**), and a stratigraphically overlying zone dominated by iron
366 sulfides (pyrite and/or pyrrhotite) with large milled clasts of surrounding lithologies (**Figs. 8e,**
367 **9l-n**). In the stratigraphically lower Zn-rich zone, abundant fine to coarse grained subhedral
368 pyrite is replaced by sphalerite (**Figs. 8d, 9l**). Anhedral quartz and Fe-chlorite are interstitial
369 to sulfide phases. Pyrrhotite is concentrated locally in the matrix. Galena is rare, and is present
370 both as rims to, and inclusions in, pyrite. Tetrahedrite locally replaces galena and exhibits
371 simple intergrowths with sphalerite.

372 In the overlying Fe-rich zone, pyrite and/or pyrrhotite are typically the dominant sulfide
373 phase with subordinate sphalerite and rare galena. Chalcopyrite inclusions occur in pyrrhotite.
374 Siliceous clasts of varying size are present in the sulfide matrix. These are well rounded and

375 represented by quartz-muscovite schist derived from the underlying footwall, or schist from
376 the stratigraphic hanging-wall (**Figs. 9m-n**). Garnet in the hanging-wall schist fragments is
377 retrogressed to chlorite (**Fig. 9n**). In drillhole EC116D, abundant fragments of chloritized and
378 deformed graphitic schist are within the massive sulfides.

379 Silicified felsic footwall rocks immediately underlying massive sulfides contain
380 veinlets of pyrite-sphalerite, which become more sphalerite poor with depth. These are often
381 strongly sheared, with trails of coarse euhedral pyrite orientated parallel to metamorphic
382 banding (**Fig. 8c**), and the contact with overlying massive sulfides (**Fig. 8d**). When present,
383 sphalerite occurs interstitially to euhedral pyrite (**Fig. 9k**), with both phases cut by veinlets of
384 galena.

385 In the chlorite-rich zone of garnet-amphibolite (**Fig. 6d**) chalcopyrite is most common
386 as blebs and stringers, along with veinlets and individual crystals of pyrrhotite and pyrite (e.g.
387 EC116D; **Figs. 8a-b**). Sphalerite crystals are often strongly deformed and may be intergrown
388 with both chalcopyrite and pyrrhotite. Ilmenite (FeTiO_3) occurs as exsolution lamellae in the
389 coarse magnetite grains, and as individual crystals in pyrrhotite (**Fig. 9b-c**). Pentlandite
390 ($[\text{Fe,Ni}]_9\text{S}_8$) is rare and is intergrown with pyrrhotite. Chalcopyrite is also intergrown with
391 pyrrhotite and fills fractures in magnetite grains (**Fig. 9c**). Drillcore logging also revealed that
392 secondary Cu minerals (predominantly malachite) are present in the uppermost sections of the
393 King deposit, most likely remobilised from the underlying Cu-bearing chloritic stockwork.

394 The immediate hanging-wall above massive sulfides can contain abundant stringers of
395 coarse euhedral pyrite (**Fig. 8g**) orientated both along the main foliation and crosscutting
396 brecciated hanging-wall lithologies.

397 **6. Geochemistry**

398 **6.1. Methods**

399 *Whole rock lithochemisrty*

400 A total of twenty-three samples of diamond drillcore from the King stratigraphy (holes
401 EC116D, EC031D, EC056D; **Fig. 6c**) were analysed for whole rock geochemistry at ALS
402 Laboratories, Perth, Australia. Major element concentrations were determined by four acid
403 digestion and ICP-OES finish on fused glass beads. Trace element, HFSE and REE
404 concentrations were determined by lithium borate fusion and ICP-MS finish. Base metals (e.g.
405 Cu, Pb, Zn, Ni) and trace metals (e.g. As, Sb, Tl, Bi) were analysed by multi-acid digestion,
406 followed by ICP-OES and ICP-AES, respectively. Carbon and S concentrations were
407 determined by total combustion using a Carbon-Sulfur Analyser, and LOI using a robotic
408 thermo-gravimetric system. Gold, Pt and Pd concentrations were analysed by fire assay and
409 ICP-OES.

410 Accuracy (%RD) was monitored using laboratory blind, mineralized and unmineralized
411 international standards (e.g. OREAS-24b – granodiorite, OREAS-620 – Golden Grove ore).
412 Precision (%RSD) was monitored by repeat analysis of submitted standard OREAS-24b

413 (granodiorite). Both precision and accuracy are considered excellent to good after Jenner
414 (1996; i.e. within $\pm 10\%$ RSD and $< 10\%$ RD) for the majority of elements from both datasets.
415 W, Li, Sn and Mo data was discarded due to poorer accuracy and/or precision than the other
416 elements (consistently $> 10\%$ RD to international standards). Thallium data was retained due to
417 excellent precision ($< 1\%$ RSD), but absolute values here should be treated with caution as
418 accuracy was poor ($> 30\%$ RD). Whole rock geochemistry results are presented in
419 **Supplementary Table 1** and plotted in **Figures 10 to 13**.

420 *Portable X-ray Fluorescence geochemistry*

421 The above whole rock geochemical data from the King deposit is complemented by
422 ~ 620 portable X-ray Fluorescence (pXRF) measurements on diamond drillcore (5 holes).
423 Portable XRF measurements were made every 0.5 to 2m of core (dependent on hole length)
424 using an Olympus InnoveX Systems Delta 2012 series model between March and May 2015.
425 The counting time was 60 seconds per analysis in soil mode. Several studies using international
426 reference materials have shown pXRF data to be precise for a number of major and trace
427 elements (e.g. [Piercey & Devine, 2014](#)). Although the accuracy of pXRF data ranges widely
428 from excellent ($< 7\%$ RD) to poor ($\pm 20\%$ RD), and often needs correcting (e.g. [Fisher et al.](#)
429 [2014](#); [Le Valliant et al. 2014](#)), downhole profiles replicate the geometry of those obtained from
430 conventional analyses ([Piercey & Devine, 2014](#)). Such data is fit-for-purpose and useful for
431 enhancing downhole geochemical trends obtained by conventional methods but should not be
432 used as a substitute for high-quality litho geochemistry ([Piercey & Devine, 2014](#)).

433 pXRF data was corrected using eleven standards from OREAS (OREAS-22d, 24b, 24c,
434 36, 38, 70b, 76b, 291, 931, 935, 991) for the following elements: As, Cr, Cu, Fe, Mn, Ni, Pb,
435 Rb, Sr, Ti, V, Y, Zn, Zr. These standards cover a wide range of concentrations for each element
436 (e.g. 38 ppm to 12.4% Cu, 4.45-23.6 wt% Fe). Calibration equations were obtained by plotting
437 certified concentrations against obtained pXRF values for each element. Only standards that
438 returned pXRF values above the limit of determination (LOD: 3x detection) were used in each
439 equation. This process was done separately for each drillhole. As an increase in pXRF machine
440 internal temperature (and consequently air pressure) is known to cause instrument drift over
441 time (due to peak positions migrating; [Fisher & Gazley, 2014](#)), standard OREAS-24b was
442 analysed every 15-20 spot analyses (total $n=71$ for 5 holes). Apart from single point anomalies,
443 instrument drift was found to be negligible and non-systematic.

444 Calibration equations used to correct pXRF data are provided in **Supplementary Table**
445 **2** along with R^2 values, which were generally excellent (most > 0.98) apart from for Cr and V
446 (which were rarely above LOD). Slight offsets between corrected pXRF and litho geochemical
447 datasets are to be expected due to the effect of spot analysis (~ 10 mm diameter) on
448 heterogeneous drillcore ([Fisher & Gazley, 2014](#)), and attenuations of elements by the plastic
449 bags in which standards were analysed (see [Fisher et al. 2014](#)). That said, these combined
450 effects appear to be minimal here for the elements of interest. Our corrected pXRF data closely
451 follow data obtained by conventional litho geochemical methods. Calculated precision and
452 accuracy data for standard OREAS-24b is presented in **Supplementary Table 3** following the
453 correction of each element. Note the excellent data quality for Sr and Rb regardless of date,

454 poorer data quality for As regardless of date, and reduced precision for all elements on the 14th
455 of May, 2015 (drillhole EC056D; most likely due to the pXRF overheating). The following
456 elements reported by the pXRF were discarded: Ag, Au, Bi, Hf, Sb, Sn, Mo, Th, U, W. These
457 were rarely above LOD and were associated with large errors (e.g. Ag \pm 9 ppm, Sb \pm 20 ppm).
458 Corrected pXRF data is presented in **Supplementary Table 4**.

459 *Magnetic susceptibility*

460 Magnetic susceptibility measurements were taken systematically every 1m of diamond
461 drillcore logged on metre marks using a Fugro RT-1 Magnetic Susceptibility Meter (~2000
462 measurements from 10 holes).

463 **6.2. Immobile element geochemistry**

464 The mobility of most of the major and trace elements during hydrothermal alteration is well
465 established in the literature (e.g. MacLean, 1990; Jenner, 1996). Only the following elements,
466 that are demonstrably immobile during both hydrothermal alteration and amphibolite-facies
467 metamorphism, are used here to elucidate petrogenesis: Al₂O₃, TiO₂, Th, Co, V, the HFSE (e.g.
468 Nb, Y, Sc) and REE (minus Eu) (Pearce & Cann, 1973; MacLean, 1990; Jenner, 1996). While
469 these elements may move on the millimetre scale during hydrothermal alteration and
470 subsequent metamorphism (as they are transferred into new minerals), they can be considered
471 immobile at the hand-specimen scale and particularly in sections of drillcore analysed here
472 (~20cm length).

473 The immobile element geochemistry of samples analysed from the King deposit is
474 illustrated in **Figures 10 and 11**. All samples of garnet-amphibolite from the footwall of the
475 deposit (and thin amphibolite units from the hanging-wall) are of calc-alkaline basaltic affinity
476 according to both the Zr/TiO₂ vs Nb/Y classification diagram of Pearce (1996; **Fig. 10a**), and
477 the Co vs Th diagram of Hastie et al. (2007; **Fig. 10d**). One exception is sample GK021, which
478 displays more intermediate geochemical characteristics (**Fig. 10a**). This is consistent with its
479 position near the overlying mixed footwall sequence (**Fig. 6c**) that is dominated by more
480 siliceous rocks. Footwall garnet-amphibolites are generally characterised by consistently high
481 Sc (17-46 ppm) and Co (84-119 ppm) concentrations, and variable Cr (<10-150 ppm) and
482 immobile element ratios (e.g. Zr/Y 2.2-12.8). Chondrite normalized REE profiles show little
483 variation between units in terms of the HREE (Dy/Yb 1.4-1.9), but there is significant LREE
484 variation in the samples analysed (La/Yb 1.7-16.5; **Fig. 11d**). This may be a consequence of
485 LREE mobility in the intensely chloritized feeder zone underlying massive sulfides (e.g.
486 Barrett & MacLean, 1994). Two samples of amphibolite analysed from the hanging-wall of the
487 King deposit (**Fig. 6c**) contain lower Co concentrations (**Fig. 10d**), higher Zr/TiO₂ ratios (**Fig.**
488 **10a**) and similar chondrite normalized HREE profiles to those from the footwall (**Fig. 11d**).

489 Rocks of intermediate composition from the mixed footwall sequence display gently
490 dipping REE profiles (La/Yb 5.8-9.1; **Fig. 11e**). Zr/TiO₂ ratios, and concentrations of Th, Sc
491 and Co are similar to overlying quartz-muscovite schists at King (**Fig. 10b**). Niobium, Y, Hf
492 and Zr concentrations are generally higher in the intermediate volcanoclastic rocks than

493 overlying felsic rocks; however, this may be a function of higher mass gain in the quartz-
494 muscovite schists, as ratio combinations of these elements yield similar values.

495 Quartz-muscovite schists from the immediate footwall of the King deposit are
496 characterised by andesitic to dacitic Zr/TiO₂ ratios (223-284; **Fig. 10b**), and calc-alkaline Zr/Y
497 (4.6-15.0) and La/Yb ratios (>9.0). Cr concentrations are below detection (<10 ppm), and Co
498 concentrations are generally low (**Fig. 10d**), both of which are consistent with a dacitic
499 protolith. Low HFSE concentrations (<5.7 ppm Hf, 5.3-15.7 ppm Y, <0.4 ppm Ta) indicate
500 these rocks are of FI (to FII) affinity (**Fig. 10e-f**). Chondrite normalized REE profiles have
501 intermediate characteristics between felsic rocks from Nimbus and Teutonic Bore (**Fig. 11f**).

502 Hanging-wall banded schists range in composition from mafic to felsic according to
503 their Zr/TiO₂ ratios and Co concentrations (**Fig. 10c, d**), consistent with their variations in
504 mineralogy (quartz-biotite dominated to amphibole±garnet) (**Fig. 7f**). Quartz-porphyry sills
505 that intrude and are interpreted as coeval with the King stratigraphy (**Fig. 6c**; labelled 1) are
506 intermediate to dacitic in composition (**Fig. 10c, d**), with high calc-alkaline Zr/Y (16.7-18.5)
507 and Th/Yb ratios, and low HFSE concentrations (**Fig. 10e-f**). Chondrite normalized REE
508 profiles are steep, both with respect to the LREE and HREE (**Fig. 11a**). The younger quartz-
509 porphyry sills (**Fig. 6c**, labelled 2) and late basaltic dykes were not analysed.

510 **6.3. Mobile element geochemistry**

511 The mobile element geochemistry of the King deposit is illustrated in **Figures 12 and 13**.
512 Regional metamorphism at King can be considered isochemical at the hand-specimen scale.
513 Although dewatering reactions during regional metamorphism may lead to the mobility of
514 volatile species (e.g. H₂S, F, CO₂; [Spry, 2000](#); [Corriveau & Spry, 2014](#)), mobile element
515 characteristics will primarily reflect hydrothermal alteration prior to metamorphism (detailed
516 in [Bonnet & Corriveau, 2007](#); [Corriveau & Spry, 2014](#)). Mass change values were not
517 calculated for samples from King as a suitable least altered precursor was not identified.
518 Weakly altered rocks analysed from Erayinia NW (eastern Murrin Domain) have distinct
519 immobile element characteristics ([Hollis et al. in prep.](#)) and are therefore not suitable for mass
520 change calculations at King, whereas those from King North are similarly altered to the rocks
521 described here ([Kelly, 2018, unpublished thesis](#)).

522 Garnet-amphibolites from the deep footwall of the King deposit are characterised by
523 high Fe₂O_{3T} (18-28 wt.%), and variable Cu (75-1315 ppm) and MgO (3-13 wt.%)
524 concentrations (**Figs. 12, 13**). This is consistent with varying degrees of Mg-metasomatism and
525 pyrrhotite-magnetite±chalcopyrite±pyrite mineralization in the feeder zone, stratigraphically
526 underlying massive sulfide mineralization (**Fig. 6d**; see Discussion). Calcium and SiO₂
527 concentrations are variable (39-51 wt.% SiO₂, 1-18 wt.% CaO) reflecting the abundance of
528 hornblende, epidote and quartz (**Fig. 12**). Sodium and K concentrations are low (<0.8 wt% for
529 each), consistent with a mafic protolith. Most pathfinder element concentrations are anomalous
530 (e.g. 2.8-15.1 ppm As, 0.3-4.2 ppm Sb) compared to unmineralized mafic rocks from the
531 Yilgarn Craton ([Hollis et al., 2015](#)), except for Tl, Bi and Au which are generally low (**Fig.**
532 **12**). Very high Mo (534 ppm) was noted in sample GK004 which is being targeted for Re-Os

533 geochronology. On the Box Plot of Large et al. (2001a) samples plot in both the ‘least altered
534 mafic’ field and between the ankerite/dolomite and chlorite/pyrite mineral nodes reflecting
535 variable enrichments in Ca, Fe and Mg.

536 Intermediate banded schists from the mixed footwall sequence show increased SiO₂
537 (58-76 wt.%) concentrations when compared to the stratigraphically underlying footwall
538 garnet-amphibolites and have highly variable K₂O (0.3-1.4 wt.%) and Na₂O (0.7-2.7 wt.%)
539 concentrations. This is consistent with the intense silicification in the mixed footwall sequence
540 (Fig. 6d), together with a more evolved precursor composition (reflected by lower TiO₂
541 concentrations; Fig. 13 - EC056D), and varying albitic alteration. Significantly lower Fe₂O_{3T}
542 (2.2-7.3 wt.%), MgO (2.8-7.4 wt.%), and Cu (3-58 ppm) reflect the decreased abundance of
543 chlorite, sulfide and magnetite present in the drillcore (e.g. EC116D: Fig. 13). Lower Ag, As,
544 Bi, Hg, Sb, and Alteration Index (A.I.) values in the intermediate rocks correlate with a
545 decreased abundance of Zn (Figs. 12, 13). All samples analysed plot with the ‘least altered
546 andesite’ field of the Box Plot (Fig. 12).

547 Quartz-muscovite schists in the immediate footwall to massive sulfides at King are
548 characterized by the highest SiO₂ (72.5-93.4 wt.%) values measured, and variable Fe₂O_{3T} (0.5-
549 6.7 wt.%) (Fig. 12). This reflects the intense silicification of host rocks and variable sulfide
550 mineralization (pyrite±sphalerite). Low Na₂O (typically ~0.3 wt), MgO (0.2-1.0 wt.%) and
551 CaO, correspond to lesser chloritic and albitic alteration, and Na-depletion though the
552 sericitization of feldspar (subsequently recrystallized to coarse muscovite during prograde
553 metamorphism). Element concentrations may have also been reduced through large mass gains
554 of SiO₂. Sample GK044 (Fig. 6c) shows significantly higher concentrations of Na₂O, CaO (4.3
555 wt.%), MgO (2.5 wt.%), and lower SiO₂ (59.8 wt.%). This sample is a coherent, weakly altered
556 dacite surrounded by sheared and intensely silica-sericite altered dacite. It most likely
557 represents a coherent lava flow or a high-level intrusion that is interbedded with volcanoclastic
558 rocks of similar composition. Hydrothermal fluids would have been preferentially focused
559 through the latter. Only sample GK044 plots within the ‘least altered dacite’ field of the Box
560 Plot with other samples trending towards the chlorite/pyrite and sericite mineral nodes (Fig.
561 12). Pathfinder elements vary in abundance in the quartz-muscovite schists, but are often high
562 (to 72ppm Cd, 465 ppm Pb, 35 ppm Sb, >25 ppm Hg) compared to all other lithologies except
563 massive sulfides (Figs. 12, 13; see following). Downhole concentrations of Ni and MnO
564 correlate well with increased amounts of Fe and base metals (Zn+Pb) in the core (EC031D:
565 Fig. 13). Arsenic concentrations increase systematically towards massive sulfides in the top
566 ~10m of quartz-muscovite schist in hole EC031D, with corresponding increases in Ag, Au, Sb,
567 Tl and positive Eu anomalies (Eu/Eu*; Fig. 13).

568 Three samples of massive sulfide were analysed from the King deposit (holes EC116D
569 and EC113D). These rocks are characterized by high Fe₂O_{3T} (24-27 wt.%) and variable Zn
570 (0.4-15.9 wt.%), reflecting the abundance of pyrrhotite, pyrite and sphalerite (Figs. 12, 13).
571 Pathfinder concentrations of the following elements are anomalous to moderately high: Ag (28-
572 50 ppm), As (40->250 ppm), Bi (2-52 ppm), Cd (95-452 ppm), Hg (>23 ppm), In (3-20 ppm),
573 Te (4-10 ppm), Sb (6->250 ppm), and Se (5-25 ppm). Lead, Cu and Au concentrations are low
574 (0.46-0.93 wt.% Pb, <125 ppm Cu, <0.1 g/t Au) compared to other VHMS deposits in the

575 Eastern Goldfields (Hollis et al. 2015). All samples display prominent positive Eu anomalies
576 (Fig. 11c). Although Sn data is considered unreliable here due to poor accuracy and precision,
577 massive sulfides have concentrations (27-112 ppm) well in excess of all other rocks analysed
578 from the King deposit (typically ~2 ppm).

579 Hanging-wall strata (both banded schists and coherent amphibolites) are characterized
580 by low SiO₂ (<57.2 wt.%). Concentrations of K₂O (0.7-1.7 wt.%), Na₂O (0.03-2.74 wt.%),
581 MgO (1.5-7.8 wt.%) and CaO (0.8-7.9 wt.%) are variable (Fig. 12). Iron concentrations are
582 high (11-24 wt.% Fe₂O_{3T}) reflecting the presence of abundant disseminated magnetite (with
583 corresponding high magnetic susceptibility) and stringer pyrite (Fig. 13). Thallium and Sb
584 concentrations are moderately high and similar to the quartz-muscovite schists adjacent to
585 massive sulfides. All samples analysed plot near the ankerite/dolomite mineral node of the Box
586 Plot due to very high CCPI, but moderate A.I. (~50%; Fig. 12). High CCPI is predominantly
587 due to the abundance of Fe, with local carbonate-alteration (Fig. 9p-r). Pathfinder
588 concentrations are typically low, except sample GK027 (with abundant stringer pyrite) that
589 contains high As (167 ppm) and Se (7.6 ppm). This sample displays the most prominent
590 positive Eu anomaly from those analysed in the hanging-wall of the King deposit (Fig. 11b).

591 7. Discussion

592 All the available evidence obtained to date is consistent with the King Zn deposit and its
593 stratigraphy representing a metamorphosed and overturned VHMS system. This model is in
594 agreement with the nature of the host rocks, grade and tonnage of the deposit, styles of
595 mineralization, the observed mineralogy of the host sequence, and its geochemical
596 characteristics. Each are discussed in turn. Finally, we discuss potential halos that may be used
597 to find VHMS deposits in amphibolite facies greenstone belts of the Yilgarn Craton.

598 7.1. Volcanic environment

599 Although the host stratigraphy of the King deposit has been metamorphosed to
600 amphibolite facies and is strongly deformed (e.g. Fig. 7e-f), its geological features are
601 consistent with an evolving volcanic sequence deposited in a deep-marine, rifted-arc or more
602 likely cratonic-rift setting. Immobile element geochemistry highlights an evolution of the
603 footwall sequence from calc-alkaline basaltic magmatism with high Co and Ti concentrations,
604 to andesitic and dacitic rocks (Figs. 10, 13) capped by massive sulfides. The return of thin
605 mafic lithologies in the hanging-wall of similar composition to the footwall (Figs. 10, 11) is
606 consistent with a shift in the geodynamic environment, possibly related to further extension
607 (Piercey, 2011). This cyclicity has been noted from many VHMS camps worldwide, with
608 mineralization occurring towards the end of a mafic to felsic eruptive cycle (Galley et al. 2007).
609 It is difficult to determine if the volcanic sequence is dominated by flow or volcanoclastic units.
610 However, recrystallised quartz clasts in the some of the mixed footwall sequence, along with
611 the broad and diffuse alteration halo associated with VHMS mineralization at King favour the
612 latter interpretation (after Gibson & Galley, 2007).

613 The presence of sulfide bearing graphitic schists at several stratigraphic horizons,
614 including the ore horizon (drillhole EC116D), are indicative of a deep marine euxinic

615 environment, below storm wave base, for the entire stratigraphy. This setting would have
616 provided a favourable chemical environment for the preservation of massive sulfides if formed
617 on the paleoseafloor. By contrast, if mineralization formed through subseafloor replacive
618 processes, fine-grained sediments may have acted to seal the hydrothermal system (Franklin et
619 al. 2005). Due to the extensive recrystallization of primary textures, it is unclear whether the
620 King deposit formed on the seafloor, or through replacive processes. The thin, sheet-like
621 morphology of massive sulfide mineralization may suggest mineralization preferentially
622 replaced a thin stratigraphic horizon, possibly of fine-grained graphitic sediments near the top
623 of the quartz-muscovite schists (as appears to be the case in EC116D; **Fig. 9I**). The presence
624 of minor sulfide mineralization (**Fig. 8g**) and the enrichment of pathfinder elements (e.g. Tl,
625 Sb) in the immediate hanging-wall (**Fig.12**) could be consistent with either a replacive model,
626 or seafloor exhalation if hydrothermal activity continued after the deposition of hanging-wall
627 strata. Further evidence for a replacive model is the presence of milled rock fragments within
628 massive sulfides (**Figs. 8e,i**). If massive sulfide mineralization formed predominantly through
629 replacive processes, these clasts may represent remnants of the unreplaced host stratigraphy
630 that were subsequently deformed during metamorphism and shearing.

631 The tectonic setting of the King stratigraphy, must be considered with regards to the
632 wider ‘arc vs plume’ debate for the origin of the Eastern Goldfields (Czarnota et al. 2010;
633 Barnes et al. 2012; Barnes & Van Kranendonk, 2014; Hollis et al. 2015, 2017a). The arc
634 scenario, used to interpret the geochemistry of rock types present in the Eastern Goldfields
635 Terrane (EGS), does not explain evidence for a common history between the Youanmi Terrane
636 and EGS, which includes: (i) contemporaneous magmatism across the EGS and Youanmi
637 Terrane from at least c. 2.82 Ga (Ivanic et al. 2010; Barnes et al. 2012); (ii) simultaneous
638 inferred ‘subduction-related’ magmatism across the whole of the craton, which is inconsistent
639 with the geometry of modern arc systems (Van Kranendonk et al. 2013); and (iii) stratigraphic
640 similarities between the Kalgoorlie and Yamarna terranes, and Youanmi and Burtville terranes
641 (Pawley et al. 2012). Furthermore, recent work has also demonstrated that mafic to felsic rocks
642 of the EGS are geochemically consistent with the fractionation of plume-related tholeiitic
643 basalts, coupled with their contamination by contemporaneous partial melts of pre-existing
644 continental crust (Barnes et al. 2012; Barnes & Van Kranendonk, 2014; Hayman et al. 2015b).
645 An arc is therefore not required.

646 Whole rock geochemical data from King are shown on the Th/Yb vs Nb/Yb plot of
647 Pearce (2008) in **Figure 10g**. The geochemical trend away from the mantle array to higher
648 Th/Yb ratios at King, favours the fractionation and crustal contamination of plume-derived
649 basaltic magmas, rather than subduction related magmatism (which would parallel the mantle
650 array; see Bédard et al. 2013). This trend is also apparent in samples analysed from Erayinia
651 NW (~4km NW of King in the Murrin Domain; Hollis et al. in prep.) and at King North (Kelly,
652 2018, unpublished thesis). Magmatic activity inferred to be plume-related precedes all episodes
653 of VHMS mineralization in the Youanmi Terrane (at c. 2.9 Ga, 2815 Ma, 2750 Ma and 2720
654 Ma; see Hollis et al. 2015). This plume-related activity is reflected by the repeated occurrence
655 of komatiitic or high-Mg basaltic magmatism in the Youanmi Terrane, followed by the eruption
656 and emplacement of major extrusive/intrusive mafic suites, terminated by felsic volcanism (van

657 Kranendonk et al. 2013; Ivanic et al. 2010) that hosts VHMS deposits (reviewed in Hollis et
658 al. 2015, 2017b). Although the age of the King deposit is not clear, the presence of komatiite
659 and BIF in the local area (see Regional Geology of Erayinia) may suggest it is of similar age
660 to the Nimbus and Anaconda deposits of the Eastern Goldfields (~2705 Ma; Hollis et al., 2015,
661 2017b).

662 7.2. Deposit type, style, grade and tonnage

663 There are over 800 significant (>0.2 Mt) VHMS deposits worldwide, mostly of small
664 tonnage (Galley et al. 2007; Piercey et al. 2015). Metal ratios reflect the tectonic setting at the
665 time of mineralization, as metals are derived through the leaching of underlying strata with
666 magmatic inputs in arc/backarc environments (Franklin et al. 2005; Galley et al. 2007; Piercey,
667 2011). Deposits may be classified as Cyprus-, Besshi-, Noranda-, Kuroko- and Bathurst-types,
668 corresponding to the nature of their host rock sequences and dominant metals (i.e. mafic Cu-
669 Zn, mafic-siliciclastic Cu-(Co-Zn-Ni), bimodal mafic Cu-Zn-Pb-(Ag-Au), bimodal-felsic Zn-
670 Pb-Cu-(Au-Ag), and felsic-siliciclastic Zn-Pb-Cu-(Au-Ag) groups respectively; Franklin et al.
671 2005; Piercey, 2011). A sixth VHMS type (i.e. Eskay Creek-type), rich in precious metals,
672 reflects hybrid deposits with both VHMS and shallow water epithermal characteristics
673 (Piercey, 2011).

674 Equivalents to most of these VHMS types are present in the Yilgarn Craton. The
675 Teutonic Bore, Jaguar and Bentley deposits of the Kambalda Terrane (**Fig. 1**) occur in mafic
676 dominated volcanic sequences, with felsic volcanic complexes and deep-marine argillaceous
677 sedimentary rocks near the ore horizon (Hallberg & Thompson, 1985; Belford et al. 2015).
678 Although these deposits are relatively small (1.6 to 3.05 Mt), Zn grades are high (9.8 to 11.3%)
679 and significant amounts of Cu are present (2 to 3.5%) with minor Pb (~0.6%). The Teutonic
680 Bore deposits therefore closely resemble bimodal-mafic or Noranda-type deposits worldwide
681 (median 3.0 Mt at 5.2% Zn, 1.7% Cu, 0.9% Pb; Piercey et al. 2015). Bimodal-felsic or Kuroko-
682 type deposits are typically characterised by significantly higher Pb (~1.9%) and lower Cu
683 (~1.4%) concentrations (Piercey et al. 2015; Yeats et al. 2017), but are more common in
684 Palaeozoic volcanic sequences than the Archean (Huston et al. 2010). Examples of felsic-
685 siliciclastic and hybrid-epithermal deposits in the Yilgarn Craton include the Hollandaire
686 (Hayman et al. 2015a) and Nimbus deposits (Hollis et al. 2017a).

687 The current King deposit resource (2.15 Mt at 3.47% Zn), while significantly smaller
688 than VHMS deposits in the Golden Grove camp of the Youanmi Terrane (e.g. Scuddles 10.5
689 Mt; **Fig. 1**), is of comparable size to most other resources in the Yilgarn Craton (e.g. Teutonic
690 Bore 1.68 Mt, Just Desserts 1.07 Mt, Hollandaire 2.8 Mt; Austin 1.48 Mt, Manindi 1.35 Mt;
691 see Hollis et al. 2015). The largest deposits in the Yilgarn often comprise multiple stacked
692 lenses of massive sulfides (e.g. Gossan Hill: Sharpe & Gemmell, 2001; Nimbus: Hollis et al.
693 2017a). The King deposit is classified as a metamorphosed bimodal-mafic or Noranda-type
694 VHMS deposit, due to the abundance of mafic to felsic volcanic rocks, low volume of
695 siliciclastic rocks, low Pb concentrations in massive sulfides (0.47-0.93%), and presence of
696 significant chalcopyrite in the feeder zone.

697 Within VHMS deposits worldwide a common metal zonation is often observed. In
698 bimodal-mafic deposits, feeder systems are typically dominated by Cu and Fe sulfides,
699 primarily chalcopyrite, pyrite and/or pyrrhotite (Galley et al. 2007). Overlying lenses of
700 massive sulfides become increasingly pyrite-sphalerite±(galena) rich and pyrrhotite-
701 chalcopyrite poor towards the paleo-seafloor (Galley et al. 2007). Gold and Ag may be
702 associated with Cu-rich, Zn-rich mineralization, or both (Gibson & Galley, 2007), as appears
703 to be the case at King (Fig. 13). Despite the extensive recrystallization of sulfide assemblages
704 at King, the zonation from a pyrite-sphalerite rich lens of massive sulfide, stratigraphically
705 underlain by a chloritic stockwork with abundant chalcopyrite, pyrrhotite and magnetite (Fig.
706 6c), is consistent with Noranda-type deposits if the local stratigraphy has been overturned. No
707 resource is available for Cu and Au, due to the limited assaying for Au in massive sulfides, and
708 both metals in the chloritic feeder zone. Samples analysed in this study reached 0.2 g/t Au in
709 footwall rocks and 0.1 g/t Au in massive sulfides (Sup. Table 1). Historic intercepts include
710 5m at 0.6 g/t Au (drillhole EC046D) and 5.9m at 0.3g/t Au (EC031D). Copper concentrations
711 reached 0.13% in litho geochemistry samples (in the garnet-amphibolite), with corrected pXRF
712 spot analyses reaching a maximum of 0.7%.

713 7.3. A metamorphosed hydrothermal system

714 Primary alteration minerals surrounding VHMS deposits include chlorite, sericite, carbonate,
715 quartz and pyrite, with talc, epidote, albite and kaolinite (or sometimes other clay minerals)
716 often present (Barrett et al. 2005; Galley et al. 2007; Yeats et al. 2017). In upper greenschist-
717 to amphibolite-facies metamorphic terranes, distinctive coarse grained mineral suites
718 commonly define VHMS alteration zones (Galley et al. 2007; Dusel-Bacon, 2012). These
719 minerals can include, but are not limited to: chloritoid, garnet, staurolite, kyanite, andalusite,
720 phlogopite, and gahnite (zincian spinel). The presence or absence of each of these minerals not
721 only reflect VHMS style hydrothermal alteration and P-T conditions during metamorphism,
722 but also the thermal gradient during metamorphism (Dusel-Bacon, 2012). A comprehensive
723 list of metamorphosed VHMS deposits under different conditions (e.g. greenschist, granulite,
724 blueschist), and common minerals associated with each, was given by Corriveau and Spry
725 (2014).

726 Hydrothermal alteration at King is dominated by quartz-
727 muscovite±chlorite±albite±carbonate in felsic to intermediate banded schists, and quartz-
728 epidote±chlorite±magnetite in garnet-amphibolite. Cordierite and anthophyllite also occur in
729 relatively minor amounts ($\cong 5\%$) in felsic to intermediate footwall rocks. According to
730 Corriveau and Spry (2014), the “best documented alteration types associated with
731 metamorphosed VHMS deposits are the cordierite-anthophyllite schists, commonly the
732 amphibolite facies analogues of chloritic alteration pipes” (p.181). Their distinct
733 litho geochemical signature (+Mg, +Fe, -Ca, -Na, -K) results in mineral assemblages that may
734 include cordierite, orthoamphibole/orthopyroxene, Al_2SiO_5 polymorphs, garnet, or staurolite,
735 quartz, biotite, and plagioclase, depending on P-T conditions. The aluminous minerals garnet,
736 chloritoid, staurolite and the Al_2SiO_5 polymorphs (=andalusite, kyanite, sillimanite) commonly
737 occur close to high-T alteration pipes. This reflects the enrichment of Al by leaching of alkalis

738 under high fluid/rock ratios (Dusel-Bacon, 2012). Metamorphosed phyllic, sericitic, and
739 argillic alteration zones (+K, +Mg, ±Fe, -Ca, -Na) will result in the formation of diagnostic
740 peraluminous and/or mica-rich metamorphic rocks (e.g. those unusually rich in Al₂SiO₅
741 polymorphs, cordierite, garnet, K-feldspars, and/or micas) (Corriveau & Spry, 2014).

742 At King, the abundance of silica-epidote in the footwall garnet-amphibolites is
743 consistent with typical seafloor alteration of basaltic rocks prior to metamorphism (Galley et
744 al. 2007). Prograde metamorphism of an Al-rich assemblage of basaltic rocks is also recorded
745 by the presence of abundant garnet, with hornblende and biotite. Garnet can locally form up to
746 50% of the rock (Fig. 7a – upper core), which has often retrogressed to chlorite and quartz.
747 The Cu-Fe sulfide bearing zone rich in chlorite and magnetite within the footwall garnet-
748 amphibolites is consistent with a stockwork zone that often underlie lenses of massive sulfides
749 that has been metamorphosed (Galley et al. 2007). The LREE variation in these footwall rocks
750 has also been observed in intensely chlorite-altered stockwork zones elsewhere (e.g. Barrett &
751 MacLean, 1994).

752 In overlying intermediate and felsic rocks the presence of significant Mg-rich cordierite
753 and anthophyllite may also be taken as evidence for Mg-metasomatism prior to metamorphism
754 (Barrett et al. 2005; Corriveau & Spry, 2014). Anthophyllite and cordierite are present within
755 other metamorphosed VHMS footwall rocks of the Yilgarn Craton. Anthophyllite has been
756 identified from the Just Desserts deposit (1.07 Mt at 1.82% Cu; Hassan, 2014), and in the
757 Quinns district associated with the Austin deposit (1.48 Mt at 1.39% Zn, 1.02% Cu; DURING
758 et al. 2016). Cordierite-rich rocks have been identified associated with VHMS mineralization
759 at Ravensthorpe (Witt, 1999), and Mount Gibson (Yeats & Groves, 1998).

760 The transition from chloritic and albitic alteration in intermediate lithologies to quartz-
761 muscovite alteration in the overlying dacitic rocks (with lower TiO₂ – Fig. 13) reflects
762 increased sericitization (+K, -Na, -Ca, -Mg) towards mineralization in footwall rocks prior to
763 metamorphism. The intermediate rocks analysed here are generally only weakly altered (Fig.
764 12 – see Box Plot). In the footwall quartz-muscovite schists, prograde metamorphism led to
765 the recrystallization of an assemblage most likely dominated by quartz-sericite±pyrite
766 ±(chlorite). These rocks are now dominated by fine granoblastic quartz with interstitial platy
767 muscovite. Minor epidote, garnet and hornblende became sinks for Ca, Al, Fe, Mg and Na.
768 Subsequent retrograde metamorphism is recorded by the replacement of the coarse muscovite
769 by sericite and Mg-chlorite, sericitisation of cordierite, and breakdown of garnet to chlorite and
770 quartz.

771 Most VHMS deposits worldwide metamorphosed to amphibolite facies are
772 characterized by at least one Al-rich phase (Araujo et al. 1995). As stated previously, alteration
773 assemblages containing Al-rich mineral phases are interpreted to represent the removal of SiO₂
774 and alkali elements by acidic fluids, and the residual concentration of Al₂O₃ in footwall rocks
775 prior to metamorphism (Galley et al. 2007; DURING et al. 2016). Staurolite porphyroblasts have
776 been recognized surrounding the Hollandaire deposit with garnet (Hayman et al. 2015a), and
777 at Wheatley with garnet, sillimanite and kyanite (Yeats, 2007; Hassan, 2017a) (Fig. 1).
778 Andalusite has been identified in metamorphosed sedimentary and felsic rocks from the

779 Dalgaranga greenstone belt (Superior Zn prospect; [Butt & Sergeev, 2003](#)), in altered footwall
780 rocks at Teutonic Bore (albeit in minor amounts; [Hallberg & Thompson, 1985](#)), at Hollandaire
781 (with kyanite; [Hayman et al. 2015a](#)), and the Quinns district (with kyanite; Tasman and
782 Franklin prospects: [Duuring et al. 2017](#); [Hassan, 2017b](#)) (**Fig. 1**). Minor andalusite was also
783 reported by [Sharpe & Gemmell \(2001\)](#) from the stratabound chlorite-(carbonate) alteration
784 enveloping massive magnetite and sulfide mineralization at Gossan Hill. More globally, the
785 Archean Geco deposit of the Superior Province, Canada, is a well-studied example of a
786 bimodal-mafic VHMS deposit metamorphosed to upper amphibolite facies. Ore hosting
787 lithologies now comprise muscovite-quartz±sillimanite schist, interpreted as a metamorphosed
788 sericitic alteration zone ([Dusel-Bacon, 2012](#)).

789 Research on the Kristineberg VHMS deposit of lower amphibolite facies from the
790 Skellefte district, Sweden, has shown that very different secondary assemblages such as
791 andalusite-quartz-muscovite and cordierite-chlorite-talc can both be produced from the same
792 precursor (e.g. rhyolite); and conversely the same mineral assemblages can also be produced
793 from different precursor rocks, such as a weakly altered andesite and strongly altered rhyolite
794 ([Barrett et al. 2005](#)). The authors proposed a series of reactions to explain the observed
795 mineralogy at Kristineberg (namely quartz, Mg-chlorite, muscovite, cordierite,
796 phlogopite/biotite, andalusite and pyrite). The most significant reactions here are:

- 797 1. 280 chlorite + 131 quartz → 231 cordierite + 180 anthophyllite + water
798 2. 40 chlorite + 28 sericite + 9 quartz → 33 cordierite + 32 phlogopite + 12 andalusite + 16 water
799 3. 140 chlorite + 49 sericite + 51 quartz → 141 cordierite + 56 phlogopite + 30 anthophyllite + water

800 The numbers before mineral names give the Niggli cation amounts of each mineral involved
801 in the reactions. Note that the major difference between the second and third equations is the
802 proportion of chlorite. When this is higher (eq. 3), cordierite, phlogopite/biotite, and
803 anthophyllite may be produced without andalusite ([Barrett et al. 2005](#)). This may explain the
804 prevalence of cordierite and anthophyllite (plus biotite) at King. Although we cannot rule out
805 the presence of an Al₂SiO₅ phase, none were observed in thin section or under SEM.

806 7.4. Prospectivity of felsic rocks

807 The immobile element geochemistry of felsic volcanic rocks has long been used to
808 distinguish VHMS fertile from unprospective camps ([Lesher et al. 1986](#); [Hart et al. 2004](#);
809 [Piercey, 2011](#)). Quartz-muscovite schists of dacitic composition from King display similar
810 geochemical characteristics to felsic rocks associated with VHMS deposits throughout the
811 Yilgarn Craton ([Hollis et al. 2015, 2017a](#)), but with subtle differences. VHMS associated felsic
812 rocks throughout the Yilgarn are characterized by: i) high SiO₂ in unaltered rocks; ii) tholeiitic
813 to transitional Zr/Y and La/Yb values (i.e. FII to FIII affinity: **Fig. 14b**); iii) flattish REE
814 profiles (La/Sm_{CN} <3, Dy/Yb_{CN} ~1); iv) high HFSE concentrations; v) high Sc/TiO₂ and Sc/V
815 ratios; and low Th/Yb ratios (<2) ([Hollis et al. 2015, 2017a](#)). These felsic rocks are also
816 equivalent to those which host VHMS deposits of the Pilbara Craton of Australia ([Vearncombe
817 & Kerrich, 1999](#)) and the Abitibi greenstone belt of Canada ([Barrie et al. 1993](#); **Fig. 14a**). One
818 exception is the Nimbus Ag-Zn-(Au) deposit, near Kalgoorlie, which is hosted by FI affinity
819 calc-alkaline dacite (**Figs. 11f, 14b**; [Hollis et al. 2017b](#)). Precious metal rich VHMS deposits

820 (i.e. Eskay Creek-type deposits) typically form at shallower water depths to classic Zn-Cu
821 deposits and are often hosted by 'less prospective' FI- to FII-affinity, calc-alkaline rocks
822 (Mercier-Langevin et al. 2011; Fig. 14a).

823 Although quartz-muscovite schists from King, display similar Zr/Y (4.6-15.0) and
824 La/Sm ratios to felsic rocks from Teutonic Bore, HFSE concentrations are significantly lower
825 (Fig. 10e-f; e.g. 68-236 ppm Zr) and HREE profiles are slightly steeper (Fig. 11f). While the
826 HFSE depletion in the King felsic rocks may be a function of element dilution through mass
827 gain, this would not explain higher Dy/Yb ratios. The FI (to FII) characteristics at King (Fig.
828 10e-f) might suggest reduced base metal prospectivity for the immediate area, in keeping with
829 lower grades of Zn mineralization and abundant occurrences of massive Fe-sulfides. However,
830 the geochemistry of felsic rocks further into the hanging-wall or footwall of the stratigraphy
831 has not been tested. Furthermore, at King North (Fig. 4) recent geochemical work on rock chips
832 from RC drilling (Kelly, 2018, unpublished thesis) has highlighted both FII and FIII affinity
833 felsic rocks in close proximity to Cu-Zn-Au mineralization.

834 7.5. Vectors and halos to mineralization

835 Many vectors and halos have been proposed to help locate VHMS deposits in volcanic
836 terranes subject to greenschist facies metamorphism. These are most powerful when used in
837 combination, and include: i) changes in the mineralogy and chemistry of host sequence
838 associated with the formation of quartz, chlorite, carbonate and sericite and the breakdown of
839 feldspar and volcanic glass (e.g. Na₂O depletion); ii) elevated concentrations of pathfinder
840 elements (e.g. Bi, Tl, Sb; Large et al. 2001b); iii) several alteration indices (e.g. Ishikawa,
841 Silicification, CCPI); and iv) changes in chlorite, carbonate and white mica chemistry (DURING
842 et al. 2016).

843

844 Regarding alteration mineralogy, we have already described common minerals
845 associated with metamorphosed VHMS systems. Recognition of mineral assemblages that
846 include cordierite, anthophyllite, biotite/phlogopite, and/or abundant garnet would be
847 significant in the Yilgarn Craton, in addition to Al-rich phases (i.e. kyanite, sillimanite,
848 andalusite and/or staurolite) not present at King. In Ontario, Canada, mapping of the intensity
849 and distribution of anthophyllite, cordierite, sillimanite, garnet, quartz, muscovite and
850 staurolite led to the identification of footwall alteration and the discovery of the Archean
851 bimodal-mafic Winston Lake deposit (Dusel-Bacon, 2012).

852

853 Zinc shows strong positive correlations with the following VHMS pathfinder elements
854 at King: Ag, As, Au, Bi, Cd, Eu/Eu* (Eu anomaly), Hg, In, Ni, Pb, Sb, Se, Tl. Similar VHMS
855 proximal metal enrichments of Ag, Au, Bi, Fe, In, MgO, Mo, S, Se and Te (with minor
856 enrichments in As, Cd, Mn, and V) were noted from the Quinns VHMS region by DURING et
857 al. (2017). Thallium and Sb concentrations are moderately high and similar to quartz-muscovite
858 schists immediately underlying massive sulfides (Fig. 12) and are comparable to other
859 Australian VHMS systems which display well developed halos (Large et al. 2001b). Both
860 elements show a progressive increase in abundance from the deep footwall garnet-
861 amphibolites, through the mixed footwall sequence, quartz-muscovite schists, peaking in

862 massive sulfides and decreasing again in hanging-wall strata (**Fig. 12** – Box and Whisker
863 diagrams). Although negative Eu anomalies may have been originally present as a primary
864 feature of the felsic volcanic rocks due to plagioclase fractionation, Eu is readily liberated
865 during hydrothermal alteration associated with the breakdown of feldspar at temperatures
866 >250°C (Sverjensky, 1984). This leads to prominent positive Eu anomalies in hydrothermally
867 altered and mineralized volcanic rocks, as observed at King (**Fig. 11**), Nimbus (Hollis et al.
868 2017), and other VHMS deposits in the Yilgarn (Hollis et al., 2015).

869 Chemographic ternary diagrams are useful for portraying common alteration trends in
870 metamorphosed terranes, as shown in **Figure 15** (Bonnet & Corriveau, 2007; Corriveau &
871 Spry, 2014). Whereas samples of footwall garnet-amphibolite from the King deposit plot
872 towards the garnet, chlorite and hornblende mineral nodes, samples of quartz-muscovite schist
873 plot towards the cordierite node and A' corner (i.e. Al-rich end) of the diagram (**Fig. 15a**). The
874 prior is interpreted to reflect the intense Mg-Fe metamorphism of the feeder zone, and the latter
875 both quartz±sericite±pyrite alteration and Al-enrichment through alkali leaching of felsic
876 volcanic rocks prior to metamorphism. Weakly altered samples from the mixed footwall
877 sequence and intrusive quartz-feldspar porphyries plot closer to the least altered volcanic field.
878 Data from the Teutonic Bore and Wheatley deposits are also shown for comparison (**Figs.**
879 **15b,c**). The intensity of Fe and Mg enrichment at Teutonic Bore is highlighted by the strong
880 clustering of both mafic and felsic footwall strata between cordierite and garnet. At Wheatley,
881 mineralized felsic gneisses plot towards the cordierite mineral nodes, whereas hanging-wall
882 amphibolites are weakly altered.

883
884 In metamorphosed terranes, the Mn contents of ferromagnesian minerals such as garnet,
885 biotite, staurolite, chlorite and amphibole have been observed to increase with proximity to
886 sulfide deposits, as well as the Zn content of staurolite and spinel (i.e. gahnite) (Spry, 2000;
887 Corriveau & Spry, 2014). The pink colour of garnets at King suggest they are Mn-rich (i.e.
888 spessartine). MnO concentrations in the King footwall garnet-amphibolite reach 1.3wt% in
889 sample GK021. Large Mn peaks were also identified in garnet EDS spectra. Spessartine garnet
890 porphyroblasts have been observed in hanging-wall and footwall strata surrounding VHMS
891 mineralization in the Yilgarn Craton at Hollandaire and Wheatley (Hayman et al. 2015; Hassan,
892 2017a). Elevated contents of Mn in garnet from garnetites, and Zn in spinel from aluminous
893 gneisses were recently noted from granulite-facies rocks in the central Grenville Province,
894 Canada, highlighting its potential for VHMS mineralization (Hindemith et al. 2017). Corriveau
895 and Spry (2014) have further suggested that staurolite becomes increasingly orange with Zn
896 content. This may prove useful to identify further resources at Hollandaire and other regions
897 where staurolite porphyroblasts surround mineralization (Hayman et al. 2015a).

898
899 As regional metamorphism is largely an isochemical process at the core scale,
900 combinations of indices such as Ishikawa Alteration Index (A.I.), Carbonate-chlorite-pyrite
901 Index (CCPI; Large et al. 2001a), the Silicification Index ($100 \times \text{SiO}_2 / (\text{SiO}_2 + \text{Al}_2\text{O}_3)$) and the
902 ACNK Index ($\text{Al}_2\text{O}_3 / (\text{CaO} + \text{Na}_2\text{O} + \text{K}_2\text{O})$; Grunsky, 2013) may be used to discriminate between
903 different styles of footwall alteration and help locate mineralization. Alteration indices and
904 pathfinder elements are plotted against vertical distance to mineralization at King in **Figure**

905 **16.** Zinc and Fe concentrations are erratic in footwall rocks using both lithogeochemical and
906 pXRF datasets. Vanadium concentrations are highest in the feeder zone and may be useful to
907 identify such rocks elsewhere, particularly when combined with high A.I., ACNK Index values
908 and the abundance of normative corundum (see below). Antimony, Tl, In, and Eu/Eu* remain
909 low in both footwall and hanging-wall strata, only increasing significantly within short
910 distances (10s of metres) to mineralization. These are consequently only of use for exploration
911 when elevated. The ACNK Index and A.I. are high in both the chloritic zone and directly
912 underlying massive sulfides. The Silicification Index by contrast peaks in hanging-wall strata
913 directly overlying massive sulfides.

914

915 The abundance of calculated normative corundum was used by Grunsky (2013) for
916 rocks from the Abitibi greenstone belt, Canada. When Al is in excess over (Ca+Na+K), the
917 presence of normative corundum may be interpreted as extensive alkali leaching, a
918 characteristic feature of footwall alteration associated with VHMS deposits. At King,
919 normative corundum abundance is highest in the chloritic feeder zone, but importantly is not
920 present (i.e. >0) in any hanging-wall strata regardless of composition. This reflects the lack of
921 alkali-leaching in the hanging-wall and may be a useful tool to identify hydrothermal upflow
922 zones associated with VHMS deposits, and also hanging-wall from footwall sequences.
923 Normative quartz abundance generally parallels the Silicification Index trend, but drops in
924 weakly altered hanging-wall strata.

925

926 **8. Conclusions**

927 The King Zn deposit (2.15 Mt at 3.47% Zn) occurs as a 2-5m thick stratiform lens
928 dominated by Fe sulfides, in a structurally overturned volcanic dominated sequence located
929 ~140km east of Kalgoorlie. The local stratigraphy is characterized by garnet amphibolite and
930 strongly banded intermediate to felsic schists with rare horizons of graphitic schist. Sulfide
931 mineralization is dominated by stratiform pyrite–pyrrhotite–sphalerite, with pyrite-(sphalerite)
932 and pyrrhotite–pyrite–(chalcopyrite) stringers at depth. The King deposit is classified as a
933 metamorphosed bimodal-mafic or Noranda-style VHMS deposit.

934 Footwall garnet-amphibolites are of sub-alkaline basaltic affinity, with high Co and Sc
935 concentrations, and flat chondrite-normalized HREE profiles. SiO₂, CaO, Fe₂O_{3T}, MgO and
936 Cu concentrations are highly variable, reflecting quartz–epidote±chlorite±magnetite±sulfide
937 alteration. Chlorite±magnetite alteration is most intense in the discordant Cu-bearing chloritic
938 feeder zone. Intermediate rocks are predominantly of calc-alkaline affinity and are similar to
939 andesites from elsewhere in the Kurnalpi terrane (e.g. Teutonic Bore). Although footwall
940 quartz-muscovite schists display similar Zr/Y and La/Sm ratios to felsic rocks from other
941 Archean VHMS deposits, HFSE concentrations are significantly lower and HREE profiles are
942 steeper. Hydrothermal alteration in felsic to intermediate rocks is characterized by a mineral
943 assemblage of quartz–muscovite±chlorite±albite±carbonate. Cordierite and anthophyllite are
944 locally significant and indicative of zones of Mg-metasomatism prior to metamorphism.
945 Increases of SiO₂, Fe₂O_{3T}, and depletions of Na₂O, CaO, and MgO occur in footwall quartz-
946 muscovite schists approaching massive sulfide mineralization.

947 Within all strata (including the immediate hanging-wall), the following pathfinder
948 elements are strongly correlated with Zn: Ag, As, Au, Bi, Cd, Eu/Eu*, Hg, In, Ni, Pb, Sb, Se,
949 Tl. These geochemical halos resemble less metamorphosed VHMS deposits across the Yilgarn
950 Craton, and suggest that although metamorphism leads to element mobility and mineral
951 segregation at the thin section scale, assay samples of ~20cm length are sufficient to vector to
952 mineralization in amphibolite facies greenstone belts of the Eastern Goldfields. Recognition of
953 minerals such as Mg-chlorite, muscovite, cordierite, anthophyllite, biotite/phlogopite, and
954 abundant garnet are significant, in addition to Al-rich phases (kyanite, sillimanite, andalusite
955 and/or staurolite) not present at King. Chemographic diagrams (e.g. A'KF and AFM) may be
956 used to identify and distinguish different alteration trends, along with the following alteration
957 indices: Ishikawa Alteration Index, Sericite Index, Silicification Index, ACNK Alteration
958 Index, and the abundance of CIPW normative corundum and quartz.

959 **Acknowledgements**

960 This contribution builds upon the efforts of a large number of individuals, particularly ABM
961 and CSA geologists. Chris Rosagro, David Mole and Jayson Meyers are thanked for thoughtful
962 discussions on the geology of the Erayinia region. The principal author was supported by the
963 Exploration Incentive Scheme at the Geological Survey of Western Australia, funded by the
964 Western Australian Government Royalties for Regions Program. Whole rock geochemistry
965 was funded by Black Raven Mining. Steven Hollis, Julian Menuge and Aileen Doran are
966 supported by the Irish Centre for Research in Applied Geosciences (iCRAG). iCRAG is funded
967 under the Science Foundation Ireland (SFI) Research Centres Programme (grant 13/RC/2092)
968 and is co-funded under the European Regional Development Fund. Patrick Hayman and an
969 anonymous reviewer are thanked for their constructive comments on this paper.

970 **References**

- 971 ABM Resources NL. (2008) Erayinia Project, Annual Report for the period ending 18th December,
972 2008. Unpublished report.
- 973 ABM Resources NL. (2009) Erayinia Project, Annual Report for the period ending 18th December,
974 2009. Unpublished report.
- 975 Araujo, S.M., Fawcett, J.J. & Scott, S.D. (1995) Metamorphism of hydrothermally altered volcanic
976 rocks in a volcanogenic massive sulfide deposit: the Palmeiropolis, Brazil, example. *Revista*
977 *Brasileira de Geociencias*, 25(3), 173-184.
- 978 Barley, M.E., Brown, S.J.A., Krapež, B. & Kositcin, N. (2008) Physical volcanology and geochemistry
979 of a Late Archaean volcanic arc: Kurnalpi and Gindalbie Terranes, Eastern Goldfields Superterrane,
980 Western Australia. *Precambrian Research*, 161, 53-76.
- 981 Barnes, S.J., Van Kranendonk, M.J. & Sonntag, I. (2012) Geochemistry and tectonic setting of basalts
982 from the Eastern Goldfields Superterrane, Yilgarn Craton. *Australian Journal of Earth Sciences*,
983 59(5), 707-735.
- 984 Barnes, S.J. & Van Kranendonk, M.J. (2014) Archean andesites in the East Yilgarn Craton, Australia:
985 products of plume/crust interaction? *Lithos*, 6, 80-92.
- 986 Barrett, T.J. & MacLean, W.H. (1994) Chemostratigraphy and hydrothermal alteration in exploration
987 for VHMS deposits in greenstones and younger volcanic rocks. In: Lentz, D.R. (ed) Alteration and
988 alteration processes associated with ore forming systems. *Geological Society of Canada Short*
989 *Course Notes*, 11, 433-467.

990 Barrett, T.J., MacLean, W.H. & Arebäck, H. (2005) The Paleoproterozoic Kristineberg VMS deposit,
991 Skellefte district, northern Sweden. Part II: chemostratigraphy and alteration. *Mineralium Deposita*,
992 40, 368-395.

993 Bédard, J.H., Harris, L.B. & Thurston, P.C. (2013) The hunting of the snArc. *Precambrian Research*,
994 229, 20-48.

995 Belford, S.M., Davidson, G.J., McPhie, J. & Large, R.R. (2015) Architecture of the Neoproterozoic Jaguar
996 VHMS deposit, Western Australia: implications for prospectivity and presence of depositional
997 breaks. *Precambrian Research*, 260, 136-160.

998 Beresford, S., Stone, W.E., Cas, R., Lahaye, Y. & Jane, M. (2005) Volcanological controls on the
999 localization of the komatiite-hosted Ni-Cu-(PGE) Coronet Deposit, Kambalda, Western Australia.
1000 *Economic Geology*, 100, 1457-1467.

1001 Black, L.P., Kamo, S.L., Allen, C.M., Aleinikoff, J.N., Davis, D.W., Korsch, R.J. & Foudoulis, C.
1002 (2003) TEMORA 1: a new zircon standard for Phanerozoic U–Pb geochronology. *Chemical*
1003 *Geology*, 200, 155-170.

1004 Bonnet, A-L. & Corriveau, L. (2007) Alteration vectors to metamorphosed hydrothermal systems in
1005 gneiss terranes. In: Goodfellow (ed) *Mineral Deposits of Canada: a synthesis of major deposit-types,*
1006 *district metallogeny, the evolution of geological provinces, and exploration methods*, p1035-1050.

1007 Boynton, W.V. (1984) Cosmochemistry of the rare earth elements: meteorite studies. In: Henderson
1008 (ed) *Rare element geochemistry*. Elsevier Pub. Co. Amsterdam, p63-114.

1009 Brown, S.J.A., Barley, M.E., Krapež, B. & Cas, R.A.F. (2002) The Late Archaean Melita Complex,
1010 Eastern Goldfields, Western Australia: shallow submarine bimodal volcanism in a rifted arc
1011 environment. *Journal of Volcanology and Geothermal Research*, 115, 303-327.

1012 Butt, C.R.M. & Sergeev, N.B. (2003) Dalgaranga base metal prospect, Mt. Magnet district, Western
1013 Australia. CRC Leme, CISRO Exploration and Mining, Bentley, Western Australia, 3p.
1014 <http://crclme.org.au/RegExpOre/Dalgaranga.pdf>

1015 Cabanis, B. & Lecolle, M. (1989; in French) Le diagramme La/10-Y/15-Nb/8; un outil pour la
1016 discrimination des series volcaniques et la mise en evidence des procusses de melange et/ou de
1017 contamination crustale. The La/10-Y/15-Nb/8 diagram; a tool for distinguishing volcanic series and
1018 discovering crustal mixing and/or contamination. *Comptes Rendus de l'Academie des Sciences*,
1019 Serie 2, Mecanique, Physique, Chimie, Sciences de 1, Univers, Sciences de la Terre, 309, 2023-
1020 2029.

1021 Caruso, S., Fiorentini, M., Hollis, S.P., LaFlamme, C., Baumgartner, R.J., Steadman, J. & Savard, D.
1022 (in review) The fluid evolution of the Nimbus Ag-Zn-(Au) deposit: an interplay between mantle
1023 plume and microbial activity. *Precambrian Research*.

1024 Cassidy, K.F., Champion, D.C., Krapež, B., Barley, M.E., Brown, S.J.A., Blewett, R.S., Groenewald,
1025 P.B. & Tyler, I.M. (2006) A revised geological framework for the Yilgarn Craton, Western
1026 Australia. *Western Australia Geological Survey, Record 2006/8*: 8p.

1027 Champion, D.C. & Cassidy, K.F. (2000) Granites of the northern Eastern Goldfields: their distribution,
1028 age, geochemistry, petrogenesis, relationship with mineralisation, and implications for tectonic
1029 environment. In: Cassidy, K.F., Champion, D.C., McNaughton, N.J., Fletcher, I.R., Whitaker, A.J.,
1030 Bastrakova, I.V. & Budd, A.R., AMIRA P482 report—The Characterisation and Metallogenic
1031 Significance of Archaean Granitoids of the Yilgarn Craton (Chapter 2).
1032 <http://www.doir.wa.gov.au/meriwa/reports/minexplor.PDF>.

1033 Corriveau, L. & Spry, P.G. (2014) Metamorphosed hydrothermal ore deposits. In: Scott, S.D. (ed)
1034 *Treatise on Geochemistry, Second Edition*, p175-194. DOI: 10.1016/B978-0-08-095975-7.01107-4.

1035 Czarnota, K., Champion, D.C., Goscombe, B., Blewett, R.S., Cassidy, K.F., Henson, P.A. &
1036 Groenewald, P.B. (2010) Geodynamics of the eastern Yilgarn Craton. *Precambrian Research*, 183,
1037 175-202.

1038 Dusel-Bacon, C. (2012) Petrology of metamorphic rocks associated with volcanogenic massive sulfide
1039 deposits in volcanogenic massive sulfide occurrence model. U.S. Geological Survey Scientific
1040 Investigations Report 2010-5070-C, chap 17, 10p.

1041 Duuring, P., Hassan, L., Zelic, M. & Gessner, K. (2016) Geochemical and spectral footprint of
1042 metamorphosed and deformed VMS-style mineralization in the Quinns district, Yilgarn Craton,
1043 Western Australia. *Economic Geology*, 111, 1411-1438.

1044 Fisher, L., Gazley, M.F., Baensch, A., Barnes, S.J., Cleverly, J. & Duclaux, G. (2014) Resolution of
1045 geochemical and lithostratigraphic complexity: a workflow for application of portable X-ray
1046 fluorescence to mineral exploration. *Geochemistry: Environment, Exploration, Analysis*, 15, 113-124.

1047 Franklin, J.M., Gibson, H.L., Galley, A.G. & Jonasson, I.R. (2005) Volcanogenic massive sulfide
1048 deposits. In: Hedenquist, J., Thompson, J.F.H., Goldfarb, R.J. & Richards, J.P. (eds) *Economic
1049 Geology 100th Anniversary Volume*. Littleton, CO, Society of Economic Geologists, p523-560.

1050 Gazley, M.F. and Fisher, L. (2014) A review of the reliability and validity of portable X-ray
1051 fluorescence spectrometry (pXRF) data. *Mineral Resource and Ore Reserve Estimation - The
1052 AusIMM Guide to Good Practice (2nd Ed)*, p.69-82.

1053 Galley, A.G., Hannington, M.D. & Jonasson, I.R. (2007) Volcanogenic massive sulfide deposits. In:
1054 Goodfellow, W.D. (ed). *A synthesis of major deposit-types, district metallogeny, the evolution of
1055 geological provinces, and exploration methods*. Geological Association of Canada, Mineral Deposits
1056 Division, Special Publication, 5, 141-161.

1057 Gee, R.D., Baxter, J.L., Wilde, S.A. & Williams, I.R. (1981) Crustal development in the Archaean
1058 Yilgarn Block, Western Australia, vol. 7. Geological Society of Australia, 43-56 (special
1059 publication).

1060 Gibson, H. & Galley, A. (2007) Volcanogenic massive sulphides of the Archean, Noranda District,
1061 Quebec. In: Goodfellow, W.D. (ed) *Mineral Deposits of Canada: a synthesis of major deposit-types,
1062 district metallogeny, the evolution of geological provinces, and exploration methods*. Special
1063 Publication No. 5, Mineral Deposits Division, Geological Association of Canada, p533-552.

1064 Green, D. & Schodlok, M. (2016) Characterisation of carbonate minerals from hyperspectral TIR
1065 scanning using features at 14 000 and 11 300nm. *Australian Journal of Earth Sciences*, 63, 951-957.

1066 Grunsky E.C. (2013) Predicting Archaean volcanogenic massive sulphide deposit potential from
1067 litho-geochemistry: application to the Abitibi Greenstone Belt. *Geochemistry: Exploration,
1068 Environment, Analysis*, 13, 317-336.

1069 Guilliame, J.N. (2014) Assessing the potential for volcanic-associated massive sulfide mineralization
1070 at Weld Range, using Golden Grove for comparison. Geological Survey of Western Australia,
1071 Report 141, 61p.

1072 Hallberg, J.A. & Thompson, J.F.H. (1985) Geologic Setting of the Teutonic Bore, Massive Sulfide
1073 Deposit, Archean Yilgarn Block, Western Australia. *Economic Geology*, 80, 1953-1964.

1074 Hancock, E.A., Green, A.A., Huntington, J.F., Schodlok, M.C. & Whitbourne, L.B. (2013) Hylogger-
1075 3: implication of adding thermal-infrared sensing. Geological Survey of Western Australia, Record
1076 2013/3, 24p.

1077 Hannington, M.D., de Ronde, C.E.J. & Peterson, S. (2005) Sea-floor tectonics and submarine
1078 hydrothermal systems. *Economic Geology 100th Anniversary Volume*, 111-141.

1079 Hart, T.R., Gibson, H.L. & Leshner, C.M. (2004) Trace element geochemistry and petrogenesis of felsic
1080 volcanic rocks associated with volcanogenic massive Cu-Zn-Pb sulfide deposits. *Economic
1081 Geology*, 99, 1003-1013.

1082 Hassan, L.Y. (2014) The Yuinmery volcanogenic massive sulfide prospects: mineralization,
1083 metasomatism and geology. Geological Survey of Western Australia, Report 131,65p.

1084 Hassan, L.Y. (2017a) Metamorphosed VMS mineralization at Wheatley, southwest Western Australia.
1085 Geological Survey of Western Australia, Record 2017/9, 39p.

- 1086 Hassan, L.Y. (2017b) Alteration associated with the Austin-Quinns VMS prospects, northern Yilgarn
1087 Craton. Geological Survey of Western Australia, Record 2017/10, 61p.
- 1088 Hastie, A.R., Kerr, A.C., Pearce, J.A. & Mitchell, S.F. (2007) Classification of altered volcanic island
1089 arc rocks using immobile trace elements: development of the Th-Co discrimination diagram. *Journal*
1090 *of Petrology*, 48, 2341-2357.
- 1091 Hayman, P.C., Hull, S.E., Cas, R.A.F., Summerhayes, E., Amelin, Y., Ivanic, T. & Price, D. (2015a) A
1092 new period of volcanogenic massive sulfide formation in the Yilgarn: a volcanological study of the
1093 ca 2.76 Ma Hollandaire VMS deposit, Yilgarn Craton, Western Australia. *Australian Journal of*
1094 *Earth Sciences*, 62, 189-210.
- 1095 Hayman, P.C., Thébaud, N., Pawley, M.J., Barnes, S.J., Cas, R.A.F., Amelin, Y., Sapkota, J., Squire,
1096 R.J., Campbell, I.H. & Pegg, I. (2015b) Evolution of a ~2.7 Ga large igneous province: a
1097 volcanological, geochemical and geochronological study of the Agnew Greenstone Belt, and new
1098 regional correlations for the Kalgoorlie Terrane (Yilgarn Craton, Western Australia). *Precambrian*
1099 *Research*, 270, 334-368.
- 1100 Herrmann, W., Blake, M., Doyle, M., Huston, D., Kamprad, J., Merry, N. & Pontual, S. (2001) Short
1101 wavelength infrared (SWIR) spectral analysis of hydrothermal alteration zones associated with base
1102 metal sulfide deposits at Rosebery and Western Tharsis, Tasmania, and Highway-Reward,
1103 Queensland. *Economic Geology*, 96, 939-955.
- 1104 Hindemith, M., Indares, A. & Piercey, S.J. (2017) Hydrothermally altered volcanic rocks
1105 metamorphosed at granulite-facies conditions: an example from the Grenville Province. *Canadian*
1106 *Journal of Earth Sciences*, 54(6), 622-638.
- 1107 Hollis, S.P., Yeats, C.J., Wyche, S., Barnes, S.J., Ivanic, T.J., Belford, S.M., Davidson, G.J., Roache,
1108 A.J. & Wingate, M.T.D. (2015) A review of volcanic-hosted massive sulfide (VHMS)
1109 mineralization in the Archaean Yilgarn Craton, Western Australia: Tectonic, stratigraphic and
1110 geochemical associations. *Precambrian Research*, 260, 113-135.
- 1111 Hollis, S.P., Mole, D.R., Gillespie, P., Barnes, S.J., Tessalina, S., Cas, R.A.F., Hildrew, C., Pumphrey,
1112 A., Goodz, M.D., Caruso, S., Yeats, C.J., Verbeeten, A., Belford, S.M., Wyche, S. & Martin, L.A.J.
1113 (2017a) 2.7 Ga plume associated VHMS mineralization in the Eastern Goldfields Superterrane,
1114 Yilgarn Craton: insights from the low temperature and shallow water, Ag-Zn-(Au) Nimbus deposit.
1115 *Precambrian Research*, 291, 119-142.
- 1116 Hollis, S.P., Yeats, C.J., Wyche, S., Barnes, S.J. & Ivanic, T. (2017b) VHMS mineralization in the
1117 Yilgarn Craton, Western Australia: a review of known deposits and prospectivity analysis of felsic
1118 volcanic rocks. Geological Survey of Western Australia, Report, 165, 68p.
- 1119 Huston, D.L., Pehrsson, S., Eglinton, B.M. & Zaw, K. (2010) The geology and metallogeny of
1120 volcanic-hosted massive sulfide deposits: variations through geologic time and with tectonic setting.
1121 *Economic Geology*, 105, 571-592.
- 1122 Huston, D.L., Champion, D.C. & Cassidy, K.F. (2014) Tectonic controls on the endowment of
1123 Neoproterozoic cratons in volcanic-hosted massive sulfide deposits: evidence from lead and neodymium
1124 isotopes. *Economic Geology*, 109, 11-26.
- 1125 Ishikawa, Y., Sawaguchi, T., Iwaya, S. & Horiuchi, M. (1976) Delineation of prospecting targets for
1126 Kuroko deposits based on modes of volcanism of underlying dacite and alteration haloes. *Mining*
1127 *Geology*, 26, 105-117.
- 1128 Ivanic, T.J., Wingate, M.T.D., Kirkland, C.L., Van Kranendonk, M.J. & Wyche, S. (2010) Age and
1129 significance of voluminous mafic-ultramafic magmatic events in the Murchison Domain, Yilgarn
1130 Craton. *Australian Journal of Earth Science*, 57, 597-614.
- 1131 Jenner, G.A. (1996) Trace element geochemistry of igneous rocks: geochemical nomenclature and
1132 analytical geochemistry. In: Wyman, D.A. (Ed.) *Trace Element Geochemistry of Volcanic Rocks:*

- 1133 *Applications for Massive Sulfide Exploration*. Geological Association of Canada, Short Course
1134 Notes 12, 51-77.
- 1135 Jiang, S-Y., Palmer, M.R. & Yeats, C.J. (2002) Chemical and boron isotopic compositions of
1136 tourmaline from the Archean Big Bell and Mount Gibson gold deposits, Murchison Province,
1137 Yilgarn Craton, Western Australia. *Chemical Geology*, 188, 229-247.
- 1138 Jones, S.A. (2007) Geology of the Erayinia 1:100 000 sheet. Western Australia Geological Survey,
1139 1:100 000 Geological Series Explanatory Notes, 37p.
- 1140 Kelly, J. (2018) Characterisation of the King North Volcanic Massive Sulfide Deposit, Yilgarn Craton,
1141 Australia. Unpublished 4th year undergraduate thesis. University of Southampton, UK.
- 1142 Krapež, B. & Hand, J.L. (2008). Late Archaean deep-marine volcanoclastic sedimentation in an arc-
1143 related basin: the Kalgoorlie Sequence of the Eastern Goldfields Superterrane, Yilgarn Craton,
1144 Western Australia. *Precambrian Research*, 161, 89-113.
- 1145 Laakso, K., Peter, J.M., Rivard, B. & White, H.P. (2016) Short-wave infrared spectral and geochemical
1146 characteristics of hydrothermal alteration at the Archean Izok Lake Zn-Cu-Pb-Ag volcanogenic
1147 massive sulfide deposit, Nunavut, Canada: applications in exploration target vectoring. *Economic
1148 Geology*, 111, 1223-1239.
- 1149 Large, R.R., Gemmill, J.B. & Paulick H. (2001a) The Alteration Box Plot: a simple approach to
1150 understanding the relationship between alteration mineralogy and litho-geochemistry associated with
1151 volcanic-hosted massive sulfide deposits. *Economic Geology*, 96, 957-971.
- 1152 Large, R.R., McPhie, J., Gemmill, J.B., Herrmann, W. & Davidson, G.J. (2001b) The spectrum of ore
1153 deposit types, volcanic environments, alteration halos, and related exploration vectors in submarine
1154 volcanic successions: some examples from Australia. *Economic Geology*, 96, 913-938.
- 1155 Leshner, C.M., Goodwin, A.M., Campbell, I.H. & Gorton, M.P. (1986) Trace-element geochemistry of
1156 ore-associated and barren, felsic metavolcanic rocks in the Superior province, Canada. *Canadian
1157 Journal of Earth Sciences*, 23, 222-237.
- 1158 Le Valliant, M., Barnes, S.J., Fisher, L., Fiorentini, M.L. & Caruso, S. (2014) Use and calibration of
1159 portable X-ray fluorescence analysers: application to litho-geochemical exploration for komatiite-
1160 hosted nickel sulfide deposits. *Geochemistry: Exploration, Environment, Analysis*, 14, 199-209.
- 1161 MacLean, W.H. (1990) Mass change calculations in altered rock series. *Mineralium Deposita*, 25, 44-
1162 49.
- 1163 McConachy, T.F., McInnes, B.I.A. & Carr, G.R. (2004) Is Western Australia intrinsically impoverished
1164 in volcanogenic massive sulfide deposits or under explored? In: McConachy, T.F. & McInnes, B.I.A.
1165 (eds). Copper-zinc massive sulfide deposits in Western Australia. CSIRO Explores 2, 15-32.
- 1166 McDonough, W.F. & Sun, S.S. (1995) The composition of the Earth. *Chemical Geology*, 120, 223-253.
- 1167 McLeod, R.L., Gabell, A.R., Green, A.A. & Gadavski, V. (1987) Chlorite infrared spectral data as
1168 proximity indicators of volcanogenic massive sulfide mineralisation: Pacific Rim Congress 87, Gold
1169 Coast, Queensland, August 26, 1987, p321-324.
- 1170 Mercier-Langevin, P., Hannington, M.D., Dubé, B. & Bécu, V. (2011) The gold content of
1171 volcanogenic massive sulfide deposits. *Mineralium Deposita*, 46, 509-539.
- 1172 Mole, D.R., Fiorentini, M.L., Cassidy, K.F., Kirkland, C.L., Thebaud, N., McCuaig, T.C., Doublier,
1173 M.P., Durning, P., Romano, S.S., Maas, R., Belousova, E.A., Barnes, S.J. & Miller, J. (2014) Crustal
1174 evolution, intra-cratonic architecture and the metallogeny of an Archaean craton. In: Jenkin, G.R.T.,
1175 Lusty, P.A.J., McDonald, I., Smith, M.P., Boyce, A.J., Wilkinson, J.J. (eds) Ore Deposits in an
1176 Evolving Earth. Geological Society, London, p.393 (special publication).
- 1177 Myers, J.S. (1990) Precambrian tectonic evolution of a part of Gondwana, southwestern Australia.
1178 *Geology*, 18, 537-540.
- 1179 Nasdala, L., Hofmeister, W., Norberg, N., Martinson, J.M., Corfu, F., Dörr, W., Kamo, S.L., Kennedy,
1180 A.K., Kronz, A. & Reiners, P.W. (2008) Zircon M257-a Homogeneous Natural Reference Material

1181 for the Ion Microprobe U-Pb Analysis of Zircon. *Geostandards and Geoanalytical Research*, 32,
1182 247-265.

1183 Nelson, D.R. (1995) 104973: metadacite porphyry, east of Liberty Bore. In: Compilation of SHRIMP
1184 U-Pb zircon geochronology data, 1994. Western Australia Geological Survey, Record 1995/3, 158-
1185 161.

1186 Nelson, D.R. (1996) 104971: metatonalite, Round Hill. In: Compilation of SHRIMP U-Pb zircon
1187 geochronology data, 1995. Western Australia Geological Survey, Record 1996/5, 43-46.

1188 Nelson, D.R. (1997) Evolution of the Archaean granite-greenstone terranes fo the Eastern Goldfields,
1189 Western Australia: SHRIMP U-Pb zircon constraints. *Precambrian Research*, 83, 57-81.

1190 Pawley, M.J., Wingate, M.T.D., Kirkland, C.L., Wyche, S., Hall, C.E., Romano, S.S. & Doublier, P.
1191 (2012) Adding pieces to the puzzle: episodic crustal growth and a new terrane in the northeast
1192 Yilgarn Craton, Western Australia. *Australian Journal of Earth Sciences*, 59, 603-623.

1193 Pearce, J.A. (1996) A user's guide to basalt discrimination diagrams. In: Wyman, D.A. (Ed.), *Trace*
1194 *Element Geochemistry of Volcanic Rocks: Applications for Massive Sulfide Exploration*. Geological
1195 Association of Canada, Short Course Notes 12, 79-113.

1196 Pearce, J.A. (2014) Immobile element fingerprinting of ophiolites. *Elements*, 10, 101-108.

1197 Pearce, J.A. & Cann, J.R. (1973) Tectonic setting of basic volcanic rocks determined using trace
1198 element analyses. *Earth and Planetary Science Letters*, 19, 290-300.

1199 Piercey, S.P. (2011) The setting, style, and role of magmatism in the formation of volcanogenic massive
1200 sulfide deposits. *Mineralium Deposita*, 46, 449-471.

1201 Piercey, S.P. & Devine, M.C. (2014) Analysis of powdered reference materials and samples by portable
1202 X-ray fluorescence spectrometer: performance and application to litho geochemistry. *Geochemistry:*
1203 *Exploration, Environment, Analysis*, 14, 139-148.

1204 Piercey, S.J., Paradis, S., Murphy, D.C. & Mortensen, J.K. (2001) Geochemistry and paleotectonic
1205 setting of felsic volcanic rocks in the Finlayson Lake, volcanic-hosted massive sulfide district,
1206 Yukon, Canada. *Economic Geology*, 96, 1877-1905.

1207 Piercey, S.J., Peter, J.M. & Herrington, R.J. (2015) Zn-rich volcanogenic massive sulphide (VMS)
1208 deposits. In: Archibald, S.M. & Piercey, S.J. (eds) Current Perspectives on Zinc Deposits. Irish
1209 Association for Economic Geology, p37-57.

1210 Podmore, D. & James, M. (2016) E28/1228. Extension of Term Application. Submitted to Department
1211 of Mines and Petroleum. Report Ref: R014.2016 E28/1228.

1212 Rudnick, R.L. & Fountain, D.M. (1995) Nature and composition of the continental crust: a lower crustal
1213 perspective. *Review of Geophysics*, 33, 267-309.

1214 Sharpe, R. & Gemmill, J.B. (2001) Alteration characteristics fo the Archean Golden Grove Formation
1215 at the Gossan Hill deposit, Western Australia: induration as a focusing mechanism for mineralizing
1216 hydrothermal fluids. *Economic Geology*, 96, 1239-1262.

1217 Spry, P.G. (2010) Sulfidation and oxidation halos as guides in the exploration for metamorphosed
1218 massive sulfide deposits. *Reviews in Economic Geology*, 11, 149-161.

1219 Squire, R.J., Allen, C.M., Cas, R.A.F., Campbell, I.H., Blewett, R.S. & Enchain, A.A. (2010) Two
1220 cycles of voluminous pyroclastic volcanism and sedimentation related to episodic granite
1221 emplacement during the late Archean: Eastern Yilgarn Craton, Western Australia. *Precambrian*
1222 *Research*, 183, 251-274.

1223 Sverjensky, D.A. (1984) Europium redox equilibria in aqueous solution. *Earth and Planetary Science*
1224 *Letters*, 67, 70-78.

1225 Swager, C.P. (1995) Geology of the greenstone terranes in the Kurnalpi-Edjudina region, southeastern
1226 Yilgarn Craton: Western Australia Geological Survey, Report 47, 31p.

1227 Swager, C.P. (1997) Tectono-stratigraphy of the late Archaean greenstone terranes in the southern
1228 Eastern Goldfields, Western Australia. *Precambrian Research*, 83, 11-42.

- 1229 Swager, C.P., Goleby, B.R., Drummond, B.J., Rattenbury, M.S. & Williams, P.R. (1997) Crustal
1230 structure of granite-greenstone terranes in the Eastern Goldfields, Yilgarn Craton, as revealed by
1231 seismic reflection profiling, *Precambrian Research*, 83, 43-56.
- 1232 Taylor, S.R. & McLennan, S.M. (1985) *The Continental Crust: its composition and evolution.*
1233 Blackwell, Oxford.
- 1234 Van Kranendonk, M.J., Ivanic, T.J., Wingate, M.T.D., Kirkland, C.L. & Wyche, S. (2013) Long-lived,
1235 autochthonous development of the Archean Murchison Domain, and implications for Yilgarn Craton
1236 tectonics. *Precambrian Research*, 229, 49-92.
- 1237 van Ruitenbeek, F.J.A., Cudahy, T., van der Meer, F.D. & Hale, M. (2012) Characterization of the
1238 hydrothermal systems associated with Archean VMS-mineralization at Panorama, Western
1239 Australia, using hyperspectral, geochemical and geothermometric data. *Ore Geology Reviews*, 45,
1240 33-46.
- 1241 Vearncombe, S. (2010) Yilgarn volcanogenic massive sulfides. In: Wyche, S. (Ed.), Yilgarn-Superior
1242 Workshop – Abstracts, Fifth International Archean Symposium. Geological Survey of Western
1243 Australia, Record 2010/20, 47-50.
- 1244 Vearncombe, S. & Kerrich, R. (1999) Geochemistry and geodynamic setting of volcanic and plutonic
1245 rocks associated with Early Archaean volcanogenic massive sulfide mineralization, Pilbara Craton.
1246 *Precambrian Research*, 98, 243-270.
- 1247 Wagner, T., Klemd, R., Wenzel, T. & Mattsson, B. (2007) Gold upgrading in metamorphosed massive
1248 sulfide ore deposits: direct evidence from laser-ablation-inductively coupled plasma-mass
1249 spectrometry analysis of invisible gold. *Geology*, 35(9), 775-778.
- 1250 Whitney, D.L. & Evans, B.W. (2010) Abbreviations for names of rock-forming minerals. *American*
1251 *Mineralogist*, 95, 185-187.
- 1252 Wingate, M.T.D. & Bodorkos, S. (2007a) 177916: metasiltstone, Karonie Mine; Geochronology dataset
1253 665. In: Compilation of geochronology data. Western Australia Geological Survey.
- 1254 Wingate, M.T.D. & Bodorkos, S. (2007b) 177919: felsic metavolcanic rock, Urania Prospect;
1255 Geochronology dataset 666. In: Compilation of geochronology data. Western Australia Geological
1256 Survey.
- 1257 Wingate, M.T.D., Kirkland, C.L. & Bodorkos, S. (2010) Introduction to geochronology data released
1258 in 2010. Geological Survey of Western Australia, Perth.
- 1259 Wingate, M.T.D., Lu, Y., Kirkland, C.L. & Spaggiari, C.V. (2016) 182419: granite gneiss, Coonana
1260 Hill, Geochronology Record 1300. Geological Survey of Western Australia, 4p.
- 1261 Witt, W.K. (1991) Regional metamorphic controls on alteration assemblages associated with gold
1262 mineralization in the Eastern Goldfields Province, Western Australia: implications for the timing
1263 and origin of Archaean lode-gold deposits. *Geology*, 19, 982-985.
- 1264 Witt, W.K. (1999) The Archaean Ravensthorpe Terrane, Western Australia: synvolcanic Cu-Au
1265 mineralization in a deformed island arc complex. *Precambrian Research*, 96, 143-181.
- 1266 Witt, W.K. & Hagemann, S. (2012) Syn-volcanic hydrothermal alteration in the Yilgarn Craton
1267 greenstones. CET Newsletter: 28-39.
- 1268 Wyche, S., Pawley, M.J., Chen, S.F., Ivanic, T.J., Zibra, I., Van Kranendonk, M.J., Spaggiari, C.V. &
1269 Wingate, M.T.D., (2013) Geology of the northern Yilgarn Craton. In: Wyche, S., Ivanic, T.J., Zibra,
1270 I. (Eds.) *Youanmi and southern Carnarvon seismic and magnetotelluric (MT) workshop.* Geological
1271 Survey of Western Australia. Record 2013/6, pp. 31-60.
- 1272 Yeats, C.J. (2007) VHMS mineral systems in the Yilgarn – characteristics and exploration potential. In:
1273 Bierlein, F.P. (Ed.) *Proceedings of Geoconferences (WA) Inc. Kalgoorlie 07 Conference*, 65–69.
- 1274 Yeats, C.J. & Groves, D.I. (1998) The Archaean Mount Gibson gold deposits, Yilgarn Craton, Western
1275 Australia: products of combined synvolcanic and syntectonic alteration and mineralisation. *Ore*
1276 *Geology Reviews*, 13, 103-129.

1277 Yeats, C.J., Hollis, S.P., Halfpenny, A., Corona, J-C. LaFlamme, C., Southam, G., Fiorentini, M.,
1278 Herrington, R.J. & Spratt, J. (2017) Actively forming Kuroko-type volcanic-hosted massive sulfide
1279 (VHMS) mineralization at Iheya North, Okinawa Trough, Japan. *Ore Geology Reviews*, 84, 20-41.

1280
1281

1282 **List of Figures**

1283

1284 **Figure 1.** Major terrane and domain subdivisions of the Yilgarn Craton, Western Australia, showing
1285 the distribution of greenstone belts and base metal occurrences (red stars) (after [Hollis et al. 2015](#)).
1286 Significant VHMS deposits are labelled. *Domains:* B, Boorara; E, Edjudina; G, Gindalbie; L, Linden;
1287 Me, Menangina; Mu, Murrin. *Other abbreviations:* GB, greenstone belt; MB, metamorphic belt. The
1288 Teutonic Bore camp includes the Teutonic Bore, Jaguar and Bentley VHMS deposits.

1289

1290 **Figure 2.** Simplified stratigraphy of the Kalgoorlie and Kurnalpi terranes of the Eastern Goldfields
1291 (after [Czarnota et al. 2010](#)). Two main episodes of VHMS mineralization have been recognized ([Hollis](#)
1292 [et al. 2015, 2017a](#)): 1. ca. 2705 Ma: Anaconda (A), Nimbus (N), King?; 2. ca. 2690-2680 Ma: Teutonic
1293 Bore (TB), Jaguar, Bentley, Erayinia NW, Jungle Pool occurrence.

1294

1295 **Figure 3.** Regional Nd isotope variations of the Yilgarn Craton (modified after [Wyche et al. 2013](#)).
1296 The position of significant VHMS occurrences associated with the Kurnalpi paleo-rift zone
1297 (highlighted by younger depleted mantle model ages) are indicated by red stars.

1298

1299 **Figure 4.** Geological map of the central Erayinia region (modified after [Jones, 2007](#)), highlighting
1300 the position of the King deposit in the Edjudina Domain, east of the Claypan Fault.

1301

1302 **Figure 5.** Distribution of banded iron formations (BIF) and komatiites in the southern Eastern
1303 Goldfields Superterrane. The figure was derived from 2010 GSWA 1: 100 000 scale outcrop mapping,
1304 overlain on the domains of [Cassidy et al. \(2006\)](#). Also shown are U-Pb zircon age constraints from
1305 each domain, and the location of Ni-sulfide occurrences (from GeoVIEW; available at
1306 www.dmp.wa.gov.au).

1307

1308 **Figure 6. (a)** Drillhole map of the King Zn-(Cu) deposit. **(b)** Composite longitudinal section through
1309 the deposit highlighting the two Zn-rich ore lenses (after [ABM Resources NL, Annual Report 2009](#)).
1310 Zinc **(c)** Cross section showing the interpreted main geological units discussed in the text. **(d)** Cross
1311 section showing the main alteration minerals present and base-metal mineralization. Dashed lines
1312 reflect the interpreted geology illustrated in Figure 5c.

1313

1314 **Figure 7.** Representative photographs of the main lithologies observed and styles of hydrothermal
1315 alteration present at King. (a-b) Variably banded and sheared footwall garnet-amphibolite. (c)
1316 Intensely chloritized zone of footwall amphibolite containing disseminated magnetite. (d)
1317 Anthophyllite-bearing schist from the mixed footwall sequence. (e-f) Folded and banded schist from
1318 the mixed footwall sequence with individual layers composed almost entirely of quartz, muscovite and
1319 epidote. (g) Albite-rich schists from the mixed footwall sequence. (h) Intensely silicified footwall
1320 felsic rocks (quartz-muscovite schist). (i) Finely banded quartz-biotite/amphibole±garnet schists from
1321 the stratigraphic hanging-wall of the deposit. Note the variation in rock types and alteration. (j) Finely
1322 banded silicified hanging-wall schists. (k) Polymict volcanic breccia with clasts of surrounding
1323 lithologies. (l) Possible grading in drillhole EC056D (hanging-wall strata), with coarse bases and

1324 schists fining downhole. (m) Early quartz-feldspar porphyry sill intruding the King deposit
1325 stratigraphy (sample GK024; **Fig. 6c** labelled 1). (n) Late unaltered quartz-feldspar porphyry sill
1326 intruding the King deposit stratigraphy (**Fig. 6c** labelled 2). (o) Basaltic dyke most likely from the
1327 Palaeoproterozoic Widgiemooltha Dyke Suite cutting the footwall garnet-amphibolite. Varioles are
1328 often present near upper and lower contacts.

1329
1330 **Figure 8.** Representative drillcore photographs of the main styles of sulfide mineralization observed
1331 at the King deposit. (a) Stringer sulfide mineralization in the chloritic zone of the footwall garnet-
1332 amphibolite, dominated by pyrrhotite with lesser chalcopyrite. (b) Blebby and stringer chalcopyrite-
1333 pyrite mineralization in footwall-garnet amphibolite. (c) Folded pyrite-sphalerite veins within the
1334 footwall quartz-muscovite schist. (d) Contact between the quartz-muscovite schist and
1335 stratigraphically overlying massive sulfides (dominated by pyrite with lesser replacive sphalerite). (e)
1336 Cap of massive Fe-sulfides (dominated by pyrite and pyrrhotite) containing milled fragments of
1337 footwall and hanging-wall strata. (f) Recrystallized pyritic stringers in banded hanging-wall schists.
1338 (g) Stringers of coarse euhedral pyrite in hanging-wall schists directly overlying massive sulfides.
1339 Tightly folded and sheared, pyrite-rich hanging-wall schists. (i) Fault gouge within the thin (<30cm)
1340 zone of massive sulfides in northernmost diamond drillhole EC063D.

1341
1342 **Figure 9.** Photomicrographs, SEM images and chemical maps for representative samples from the
1343 King stratigraphy. (a) Footwall garnet-amphibolite with disseminated sulfides. (b) Reflected light
1344 image of sulfide and oxide phases present within footwall garnet-amphibolites (c) Chemical map of
1345 the area in Figure 8b (denoted by a white box). (d) Intensely chloritized zone of garnet-amphibolites.
1346 (e) Quartz-hornblende schist from the mixed footwall sequence (f-h) Anthophyllite bearing quartz-
1347 biotite-chlorite-albite-epidote schist from the mixed footwall sequence. (i-j) Quartz-muscovite schist
1348 from the immediate footwall of the King deposit. (k) Coarse euhedral pyrite in quartz-muscovite schist,
1349 with interstitial sphalerite. (l) Massive sulfide with sphalerite replacing pyrite and large milled clasts
1350 of surrounding quartz-muscovite schist. (m-n) Massive sulfides containing garnet porphyroblasts
1351 retrograded to chlorite. (o-r) Petrographic and SEM images of hanging-wall mafic (o,r) and felsic (p-
1352 q) strata. Drillhole numbers and sample depths are indicated by the format 116/425m. *Plane polarised*
1353 *light* – **Fig. 9a,f**; *Cross polarized light* – **Fig. 9d,e,i,j,o,p,q**; *SEM images* – **Fig. 9g,k,m,r**. *SEM*
1354 *composite chemical maps* - **Fig. 9c,h,n**. Chemical mapping was completed using a Hitachi
1355 TM3030Plus Tabletop Scanning Electron Microscope at University College Dublin, Ireland. Maps
1356 were completed over 2-3 hours each using a pixel dwell time of 800 μ s, resolution of 1024 and process
1357 time of 4 seconds. Composite colour maps were produced by merging element concentration maps of
1358 interest using the Oxford Instruments Aztec One (v. 3.2) software.

1359
1360 **Figure 10.** Immobile element geochemistry for samples analysed from the King deposit. (a-c) Zr/TiO₂
1361 vs Nb/Y discrimination diagrams for volcanic rocks (after [Pearce, 1996](#)). Probability ellipses for
1362 various rock types are shown after [Pearce \(1996\)](#). These represent 10% probability contours – that is
1363 10% of samples from that group will plot outside the respective contour. (d) Th vs Co discrimination
1364 diagram of [Hastie et al. \(2007\)](#). (e-f) VHMS fertility diagrams of [Lesher et al \(1986; Fig. 9d\)](#) and [Hart](#)
1365 [et al \(2004; Fig. 9f\)](#). Felsic volcanic rocks from Teutonic Bore are of FIII affinity characterised by
1366 high concentrations of the HFSE and low Zr/Y and La/Yb ratios. Footwall quartz-muscovite schist
1367 from King is of FI to FII affinity and less prospective for VHMS mineralization. (g) Th/Yb vs Nb/Yb
1368 diagram of [Pearce \(2008, 2014\)](#). Arc related volcanic rocks will parallel the mantle array, whereas
1369 samples trending obliquely to it are associated with crustal contamination ([Pearce, 2008](#)). 1. Yilgarn
1370 Felsic Intrusion ([Hayman et al. 2015b](#)); 2. Felsic Archean Crust ([Rudnick & Fountain, 1995](#)); 3. Upper
1371 Continental Crust ([Taylor & Mclennan, 1995](#)).

1372
1373
1374
1375
1376
1377
1378
1379
1380
1381
1382
1383
1384
1385
1386
1387
1388
1389
1390
1391
1392
1393
1394
1395
1396
1397
1398
1399
1400
1401
1402
1403
1404
1405
1406
1407
1408
1409
1410
1411
1412
1413

Figure 11. Chondrite-normalized REE profiles (after McDonough & Sun, 1995) for samples analysed from the King deposit. Shaded fields for rocks from Nimbus and Teutonic Bore are from Hollis et al. (2017) and Hollis (unpublished) respectively.

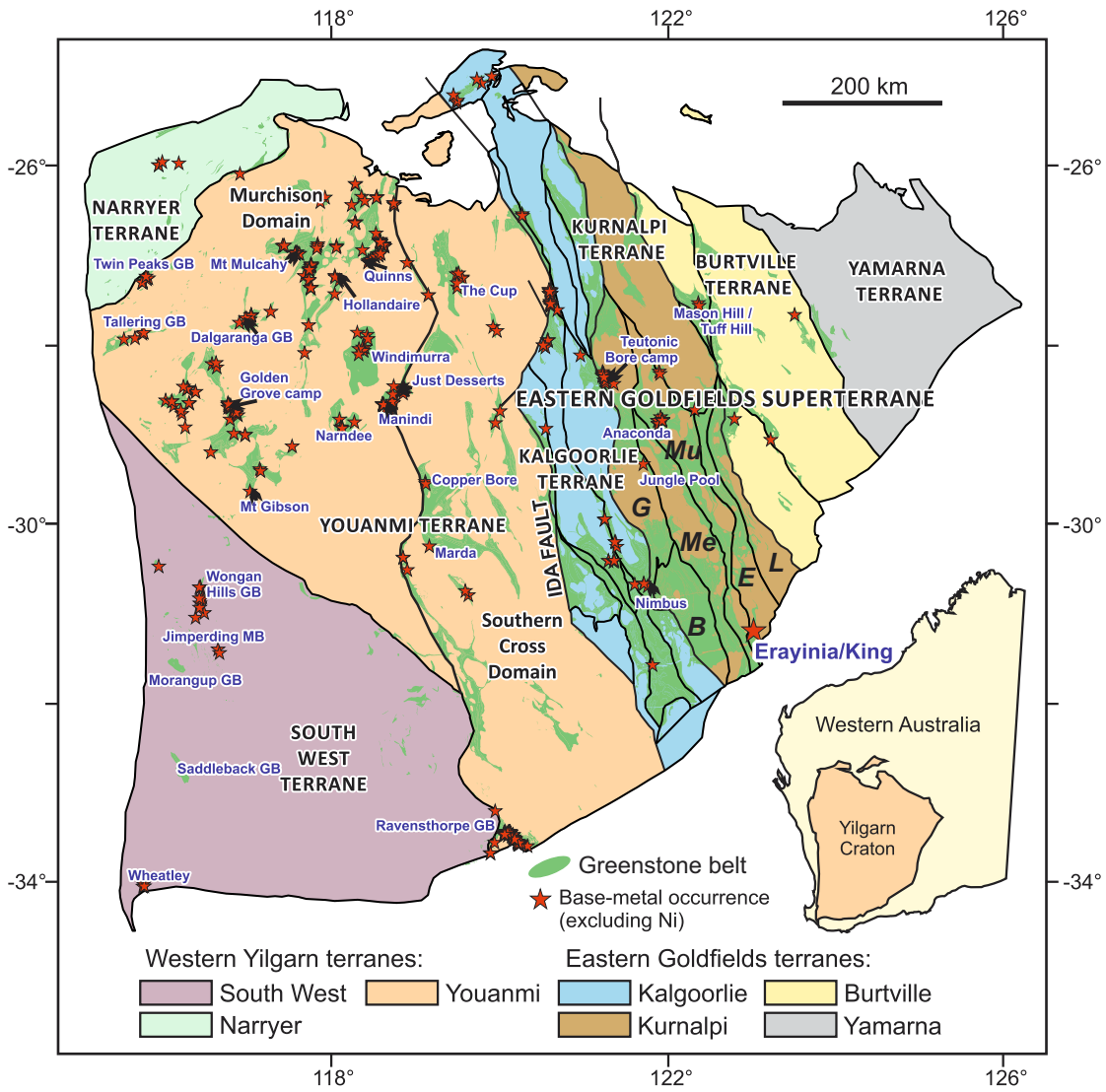
Figure 12. Mobile element geochemistry of samples analysed from King. The Box Plot (bottom left) uses both the Alteration Index (A.I.) of Ishikawa et al. (1976) and the Carbonate-chlorite-pyrite Index of Large et al. (2001a) to show common trends associated with hydrothermal alteration.
 $A.I.=100*(K_2O+MgO)/(K_2O+MgO+Na_2O+CaO)$;
 $CCPI=100*(MgO+FeO)/(MgO+FeO+Na_2O+K_2O)$.

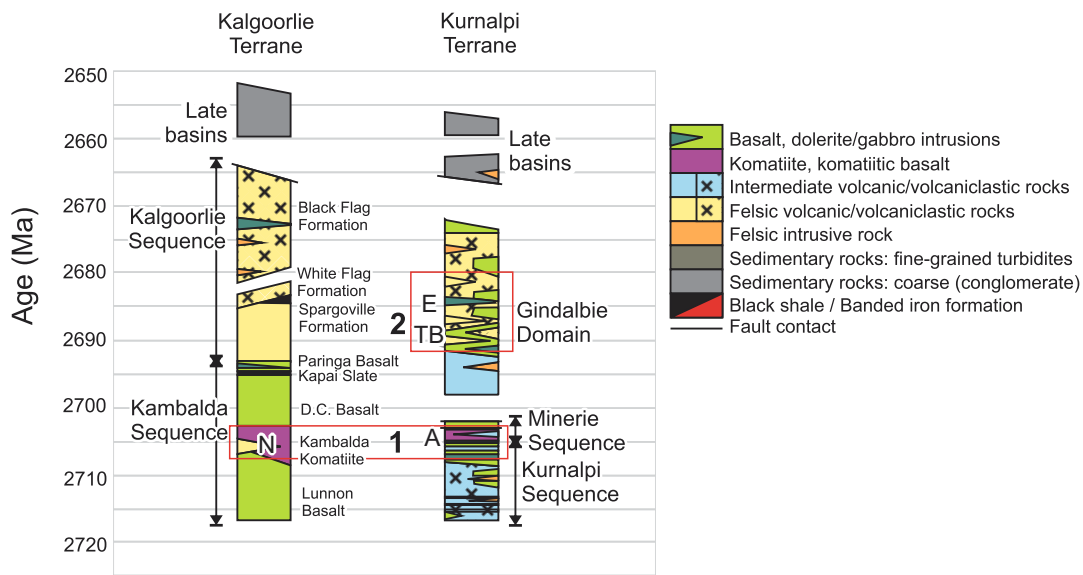
Figure 13. Downhole geochemical profiles for drillholes EC116D, EC056D and EC031D using data obtained by both the pXRF and whole rock methods (see Figure 6 for drillhole locations). Eu/Eu* calculated after Boynton (1984).

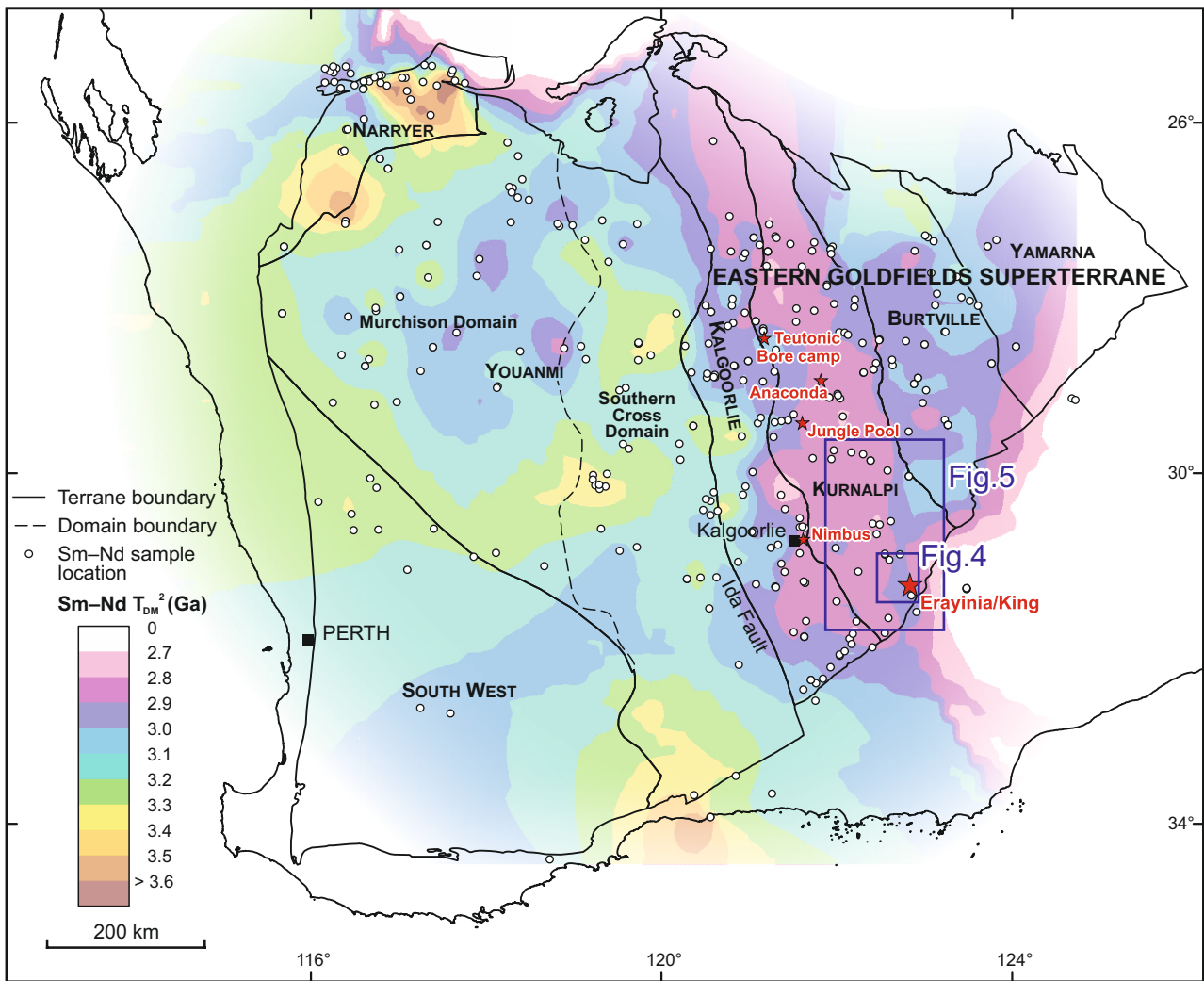
Figure 14. Prospectivity of felsic rocks from (a) the Abitibi greenstone belt, Canada, and (b) Younami Terrane, and Eastern Goldfields, according to the Zr/Y vs Y felsic discrimination diagram of Lesher et al. (1986). All stacked plots are the same scale with Zr/Y ratios for each section of the stack indicated on y-axes. Adapted from Hollis et al. (2015), with additional data from Hollis et al. (2017a – Nimbus deposit) and Hassan (2017a – Wheatley deposit).

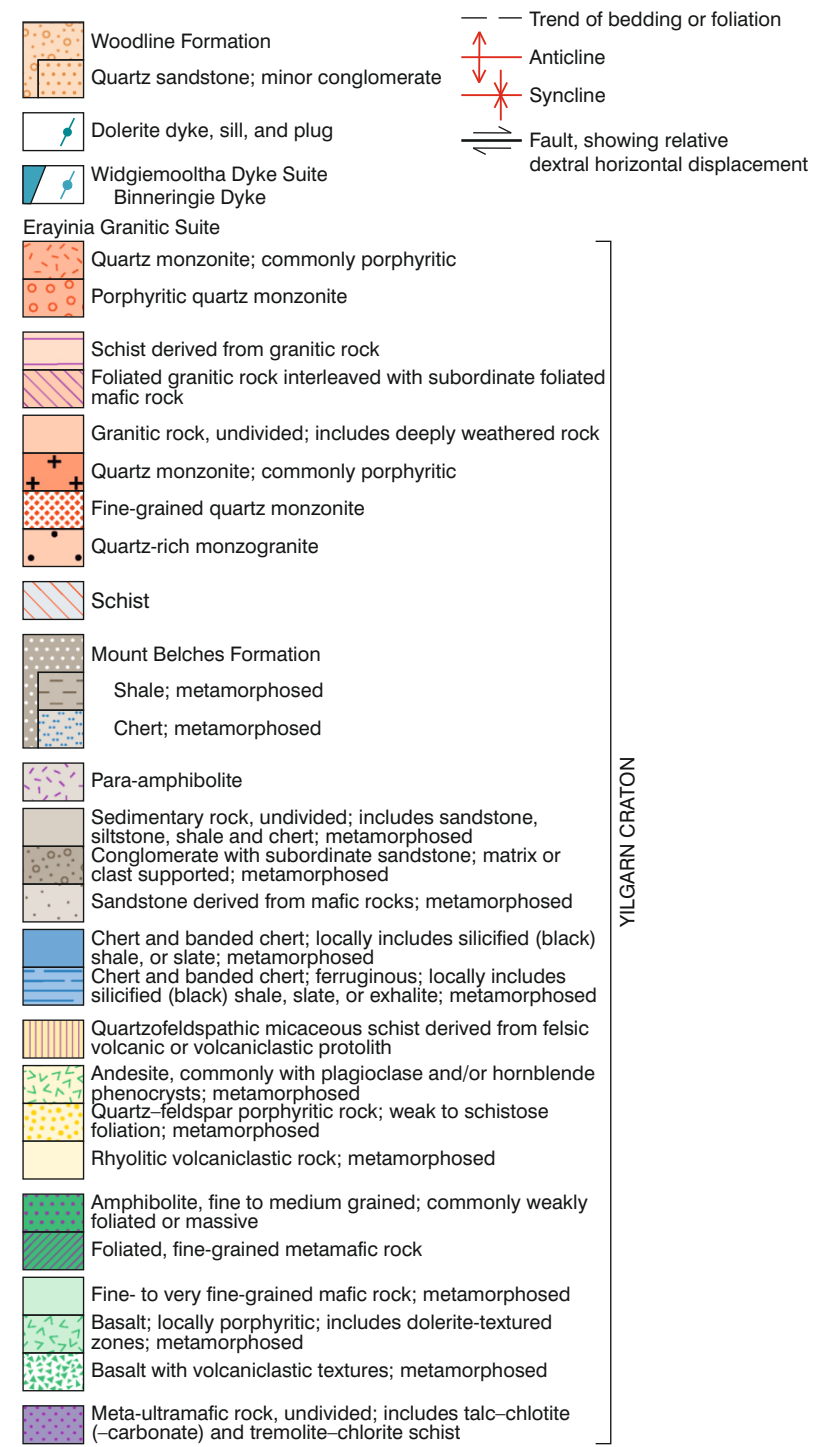
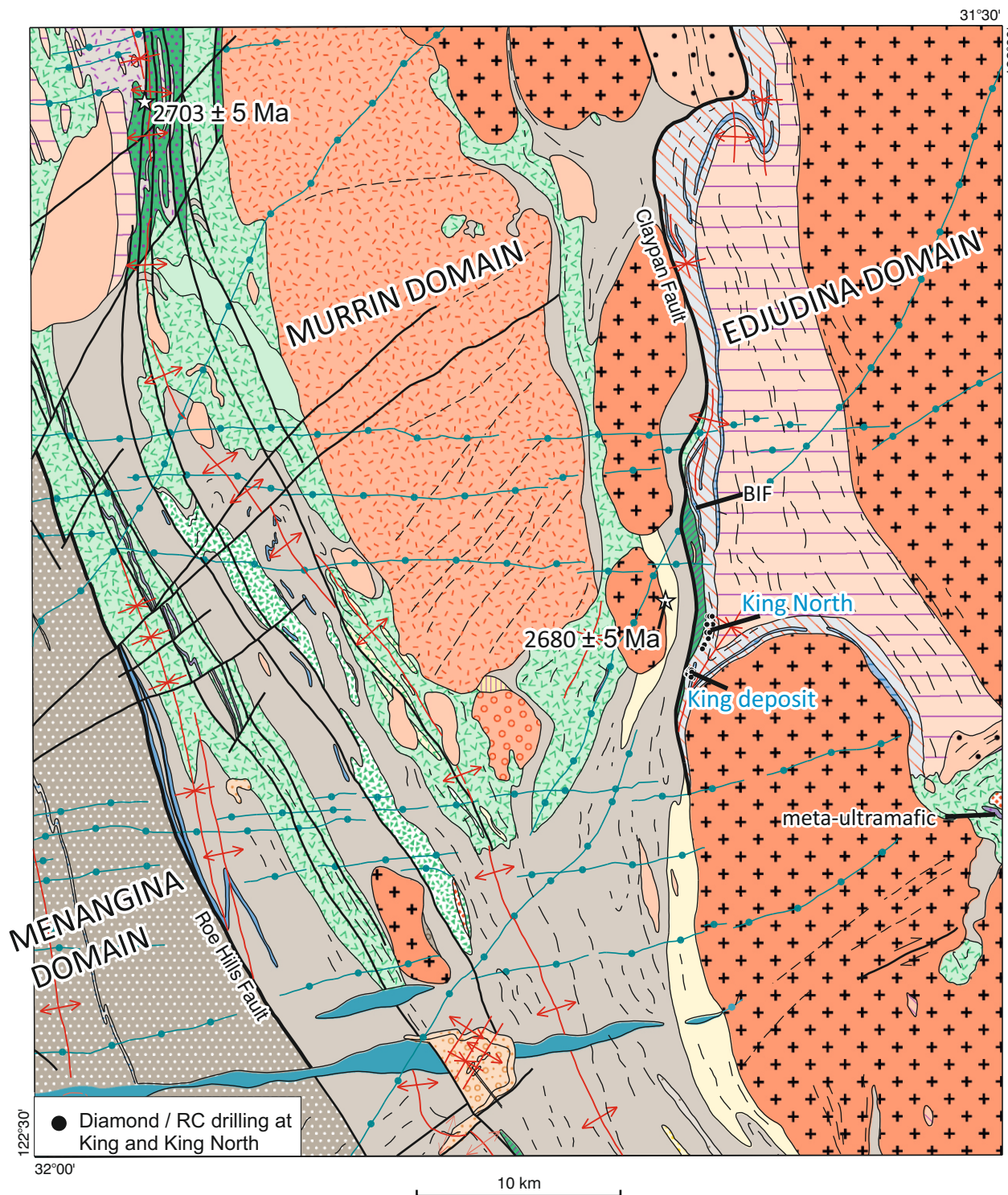
Figure 15. (a) Chemographic diagrams (A'CF, A'KF and AFM) used to portray common alteration trends and mineral nodes in metamorphosed terranes (diagrams modified after Bonnet & Corriveau, 2007; Corriveau & Spry, 2014). Samples are plotted using molecular proportions (i.e. the chemical analysis of the rock is recalculated by dividing the molecular weight of each oxide constituent by the molecular weight of that oxide). (a) King deposit, (b-c) Mafic and felsic volcanic rocks analysed from the Teutonic Bore and Wheatley VHMS deposits (data from Hollis, unpublished; Hassan, 2017a). The point density contours in 14b reflect the field of least/weakly-altered felsic and intermediate volcanic/volcaniclastic rocks from the Yilgarn Craton. This dataset, compiled by Hollis et al. (2015), was filtered to remove samples with anomalous Zn (>100 ppm) and high degrees of alteration (Silicification Index >80%). A'CF: $A'=Al_2O_3+Fe_2O_3-(K_2O+Na_2O)$, $C=CaO$, $F=FeO+MnO+MgO$. A'KF: $A=Al_2O_3+Fe_2O_3-(K_2O+Na_2O+CaO)$, $K=K_2O$, $F=FeO+MnO+MgO$. AFM: $A=Al_2O_3-K_2O$; $F=FeO$, $M=MgO$. Abbreviations for mineral names (Whitney and Evans, 2010): Act - actinolite, Alm - almandine (garnet), An - anorthite, Ath - anthophyllite, Bt - biotite, Cal - calcite, Chl - chlorite, Crd - cordierite, Di - diopside, Ep - epidote, Grs - grossular (garnet), Grt - garnet, Hbl - hornblende, Hd - hedenbergite, Kfs - K-feldspar, Ky - kyanite, Ms - muscovite, Opx - orthopyroxene, Prp - pyrope (garnet), Sil - sillimanite, Tr - tremolite.

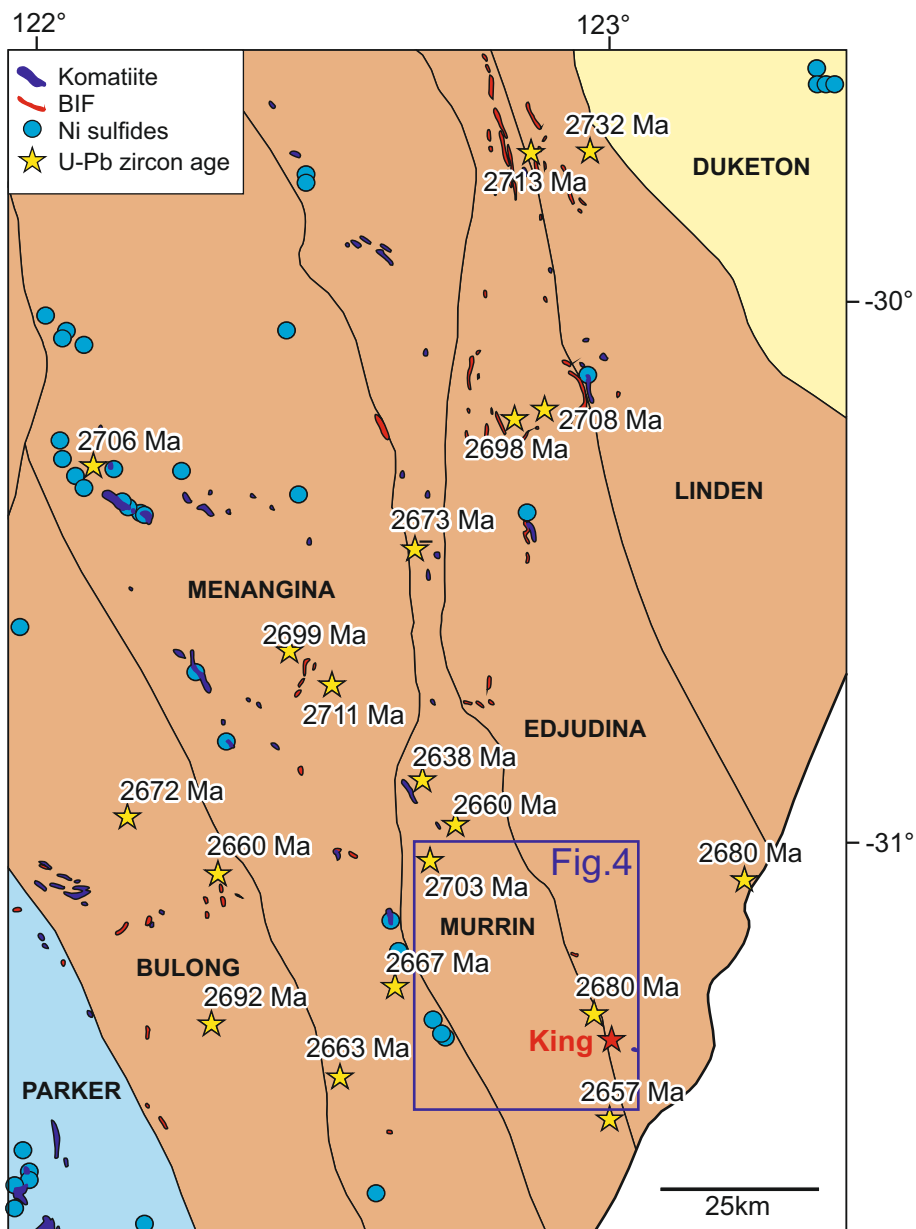
Figure 16. Geochemical and mineralogical vectors to mineralization at King, plotted as distance to massive sulfide mineralization (calculated perpendicular to ore in section 6538650mN; Fig. 6c). Normative CIPW quartz and cordierite abundances (volume %) were determined using the Norm 4 spreadsheet of Kurt Hollocher (Union College).

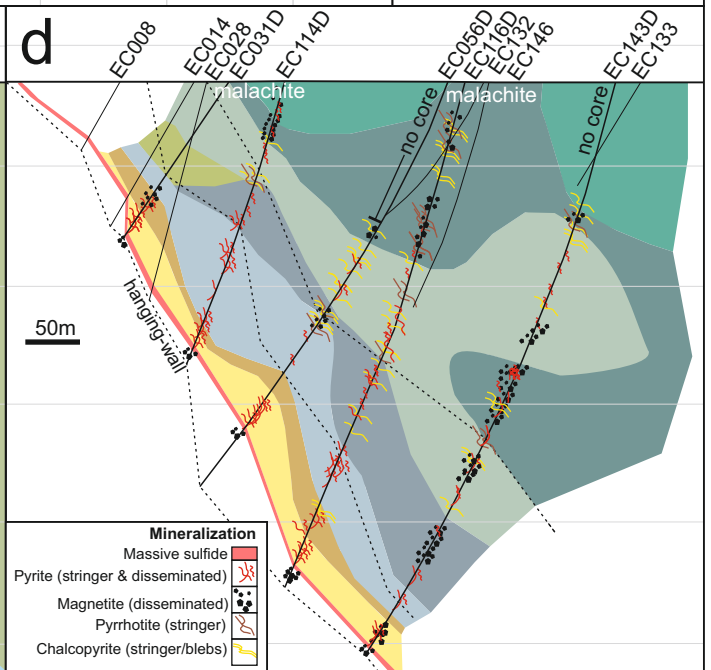
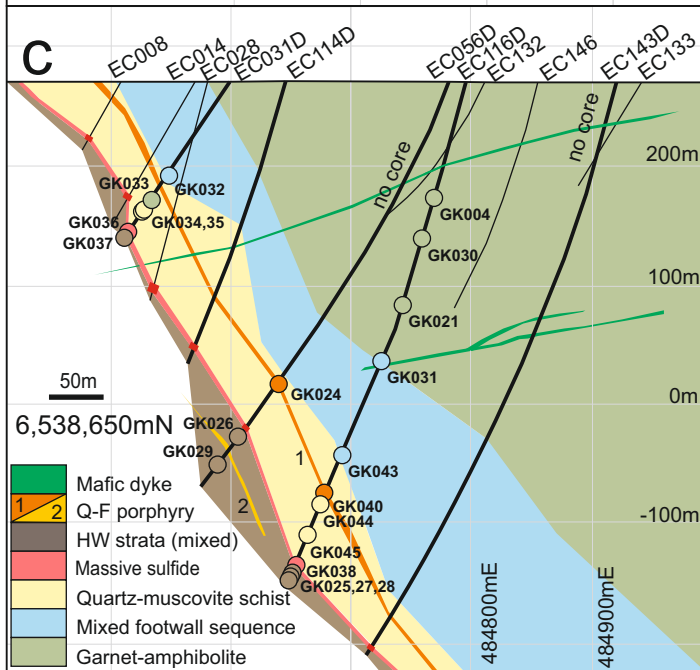
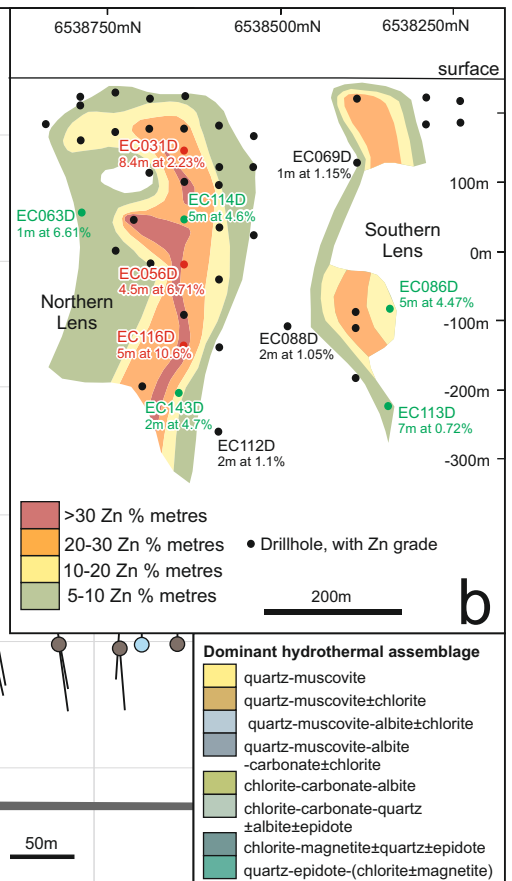
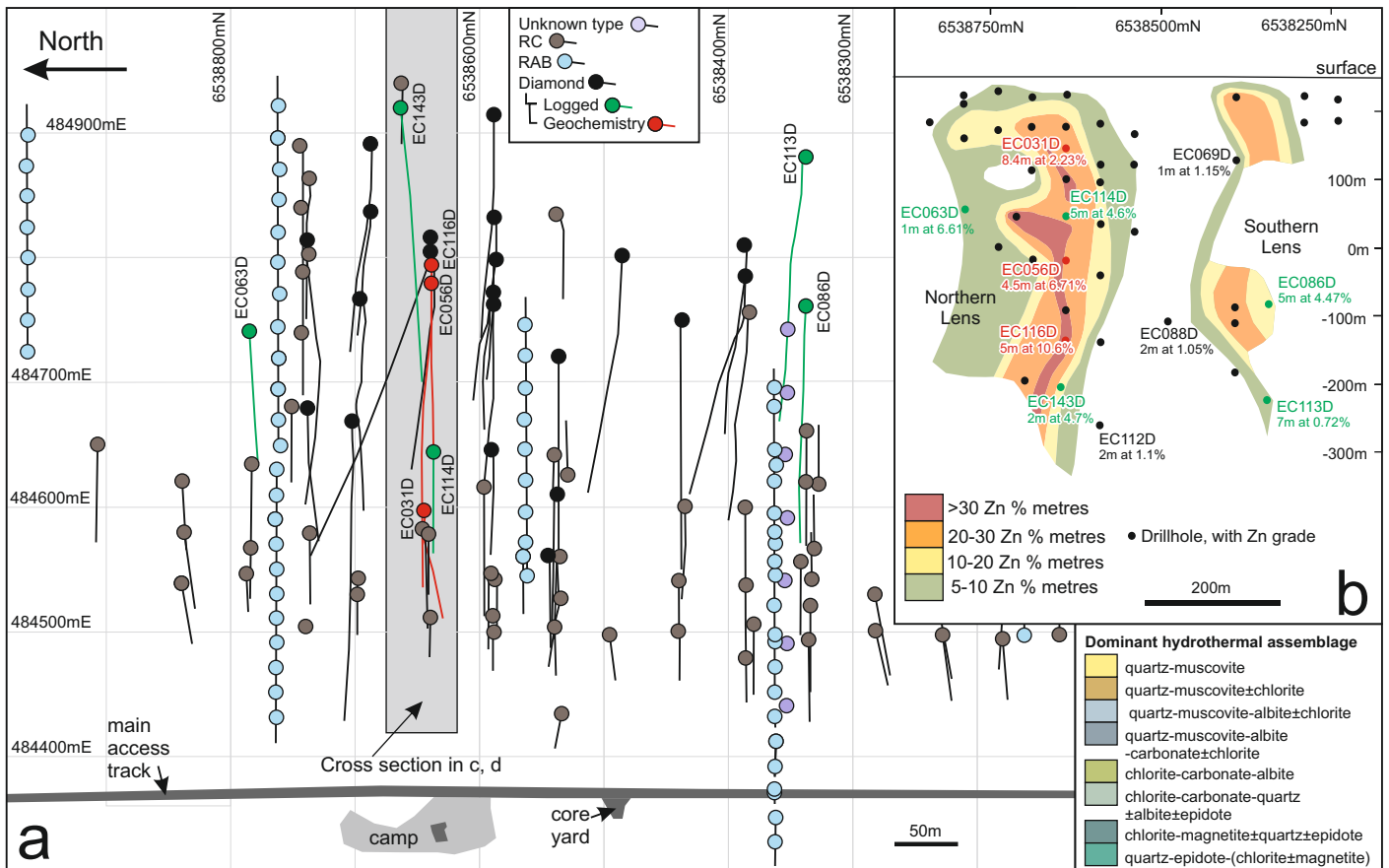


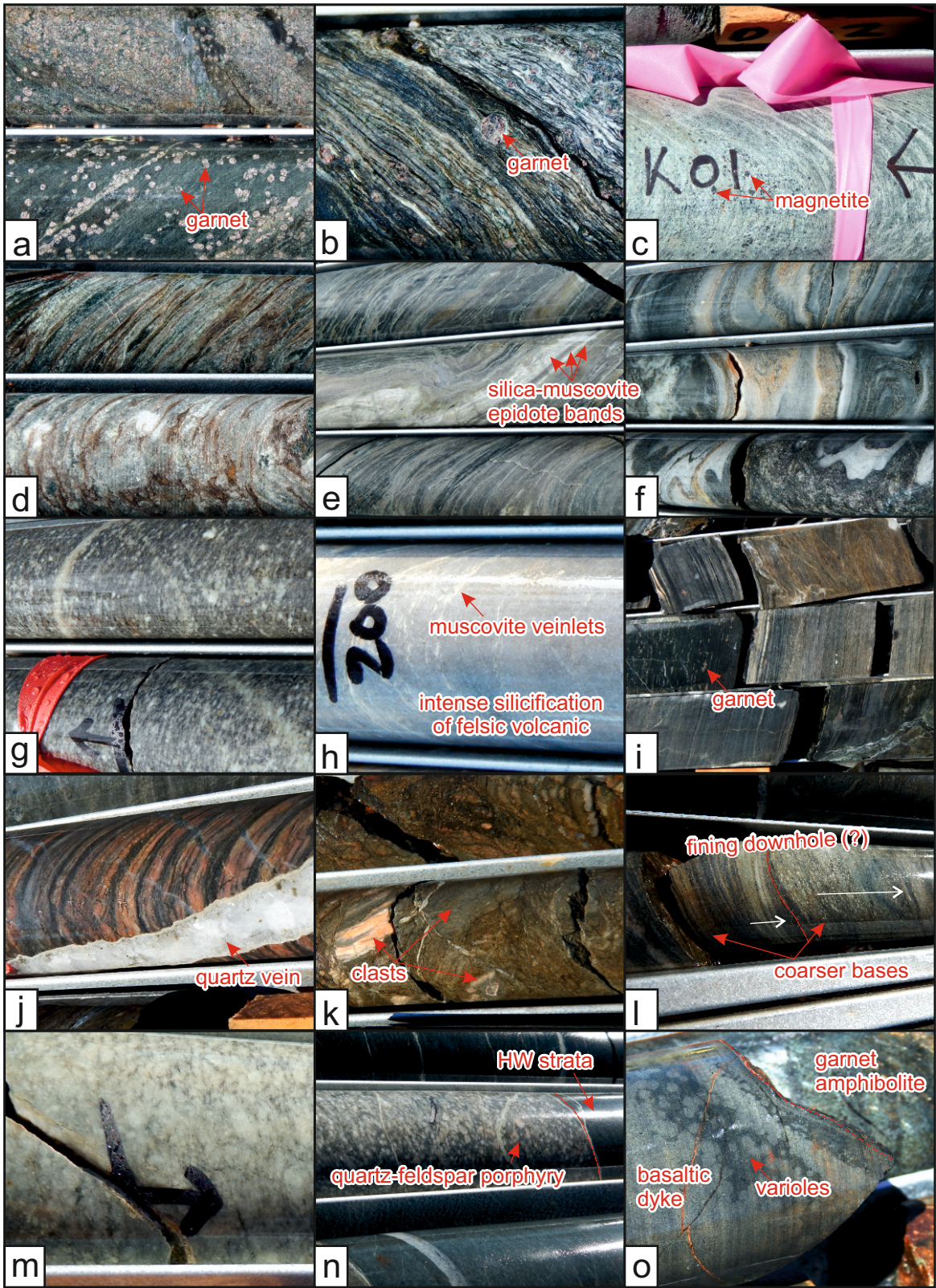


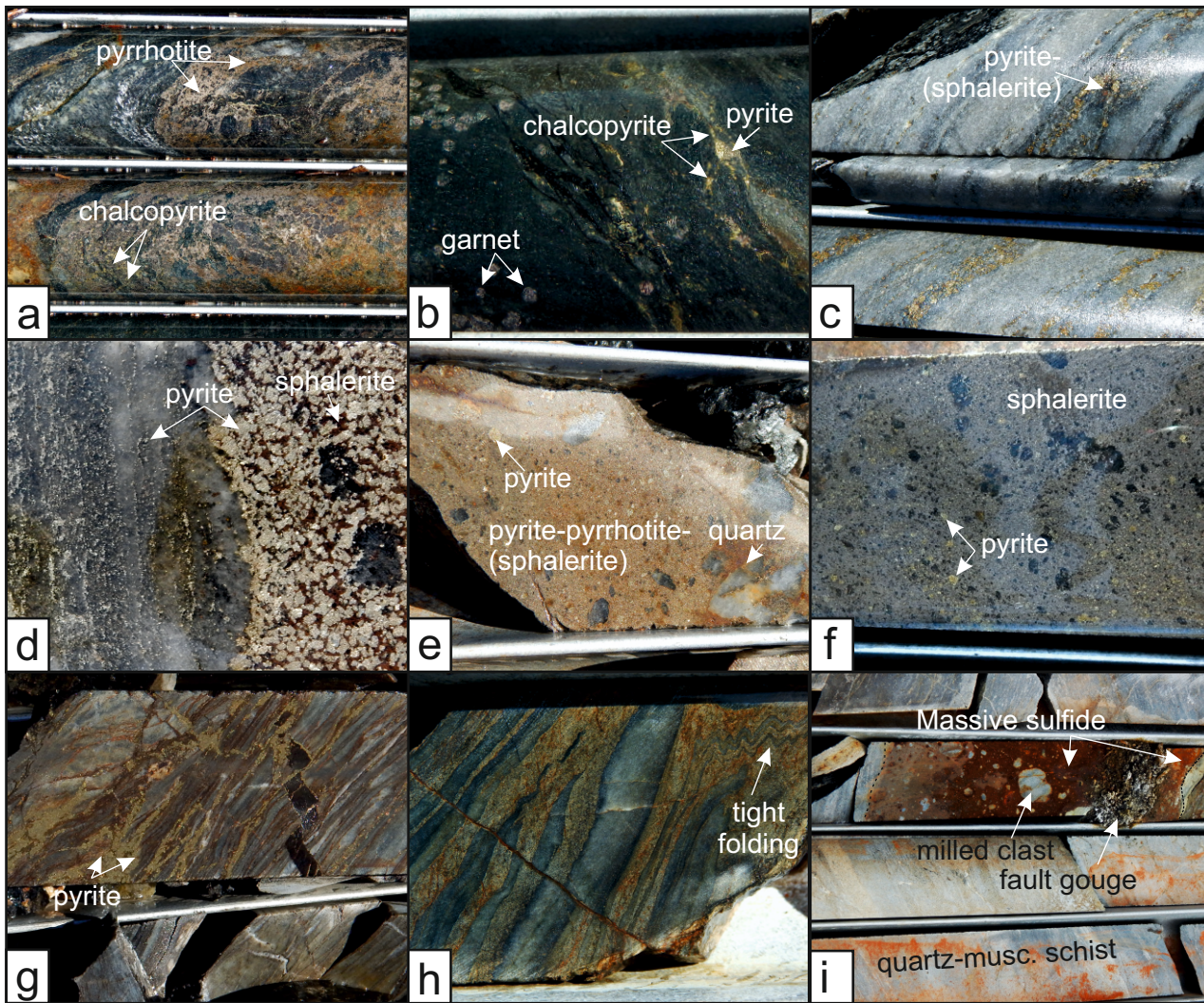


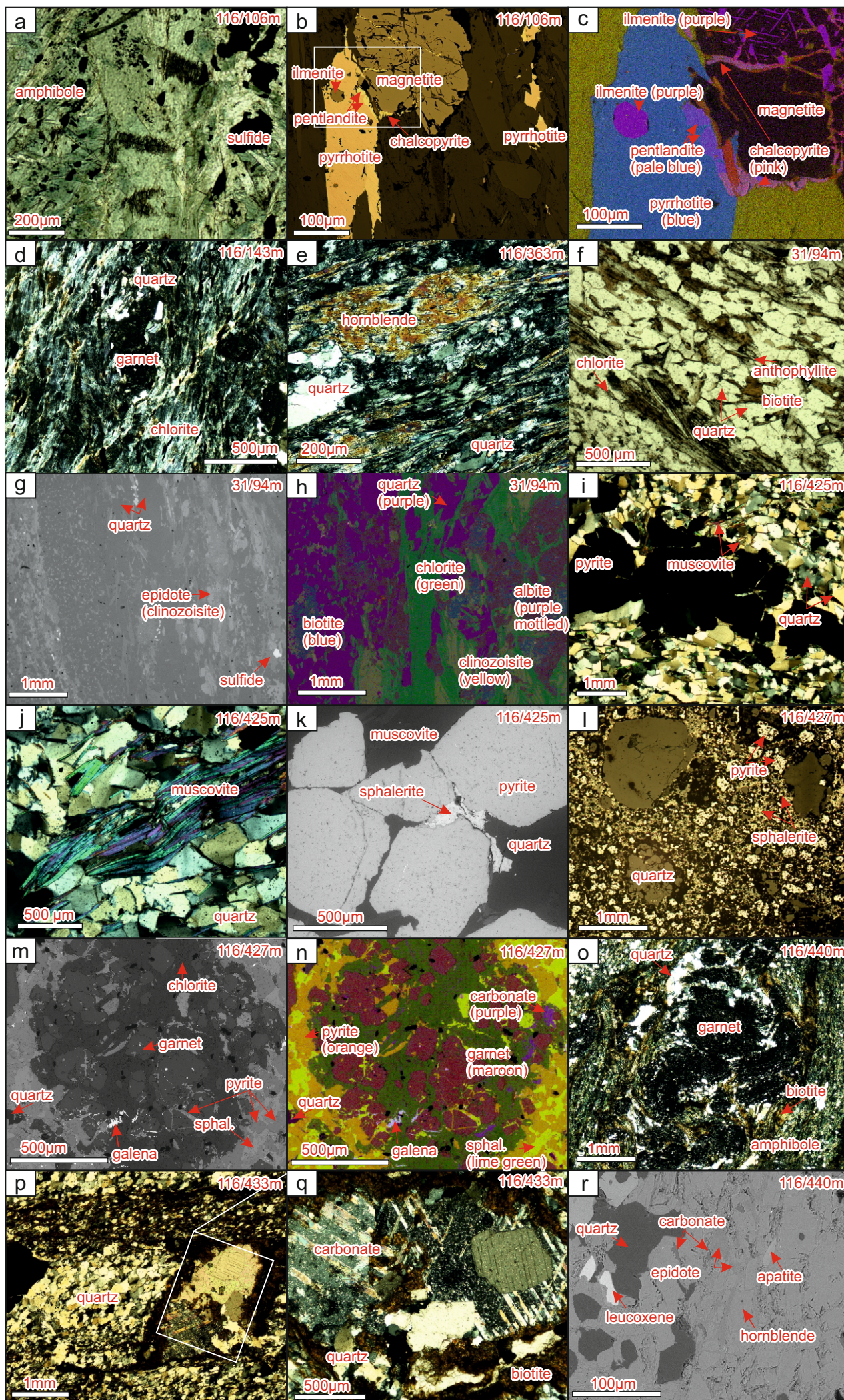


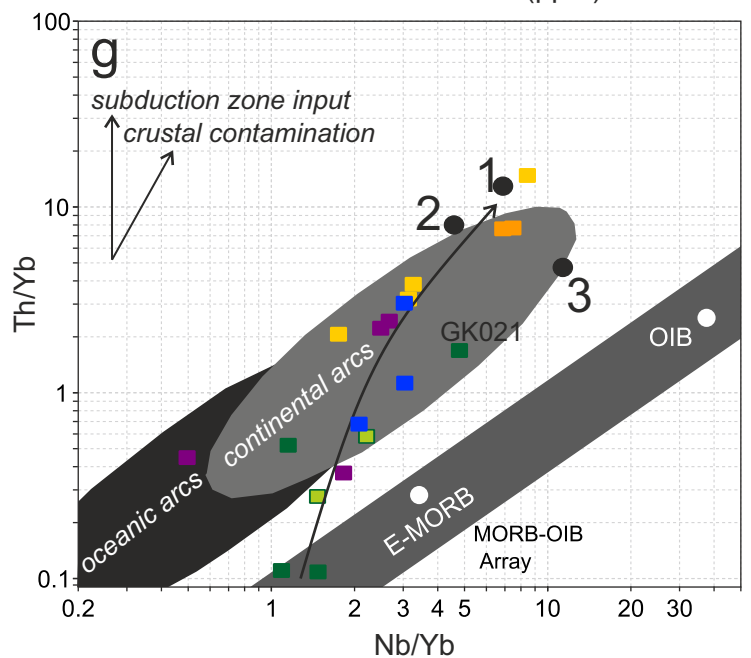
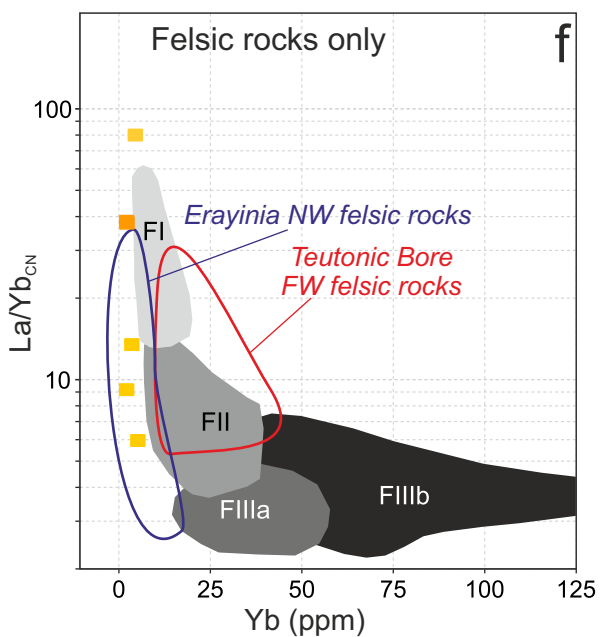
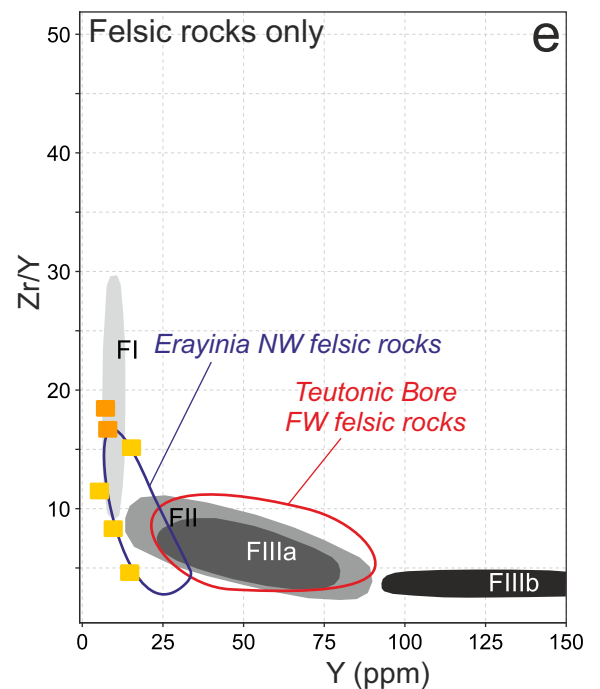
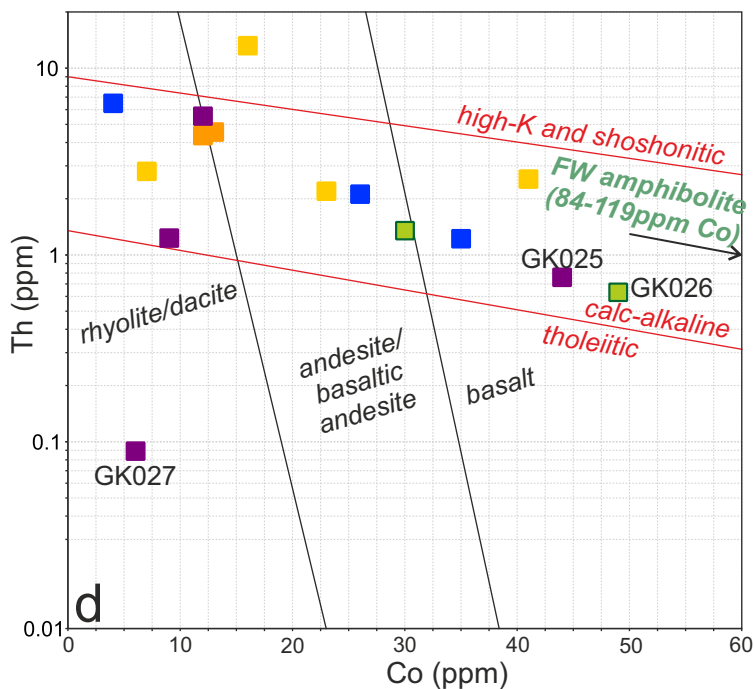
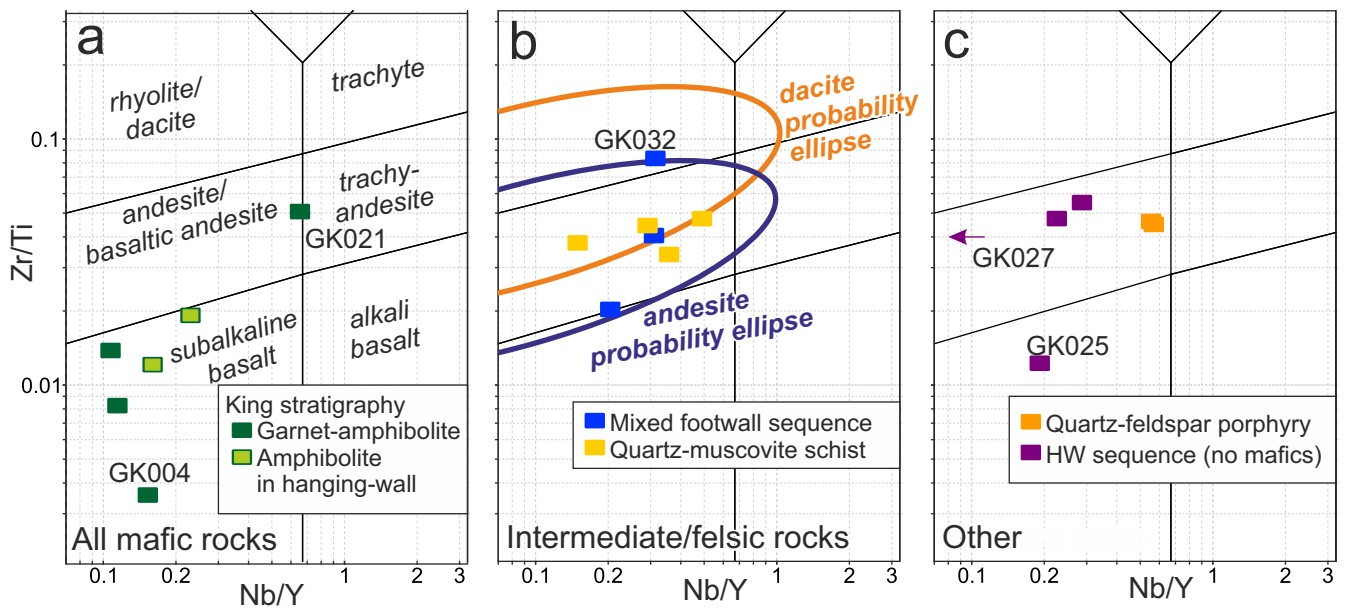


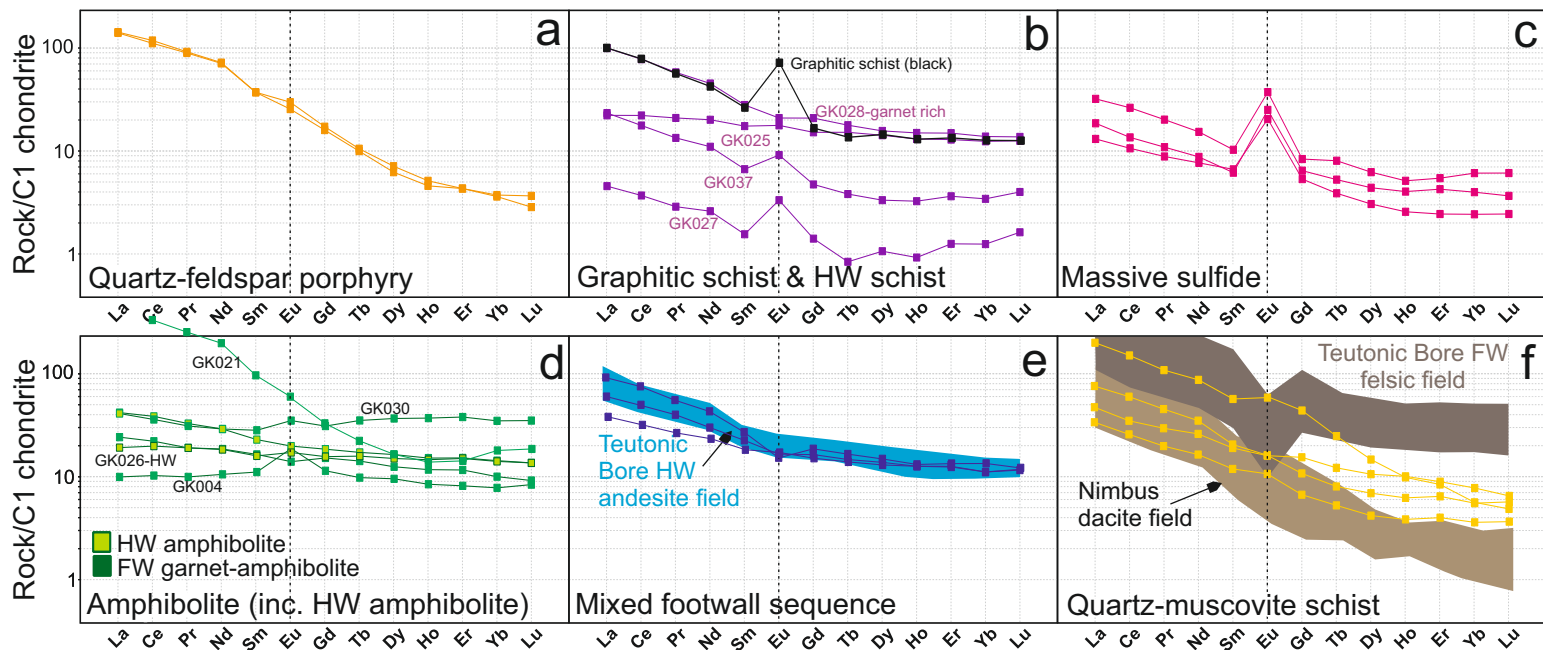


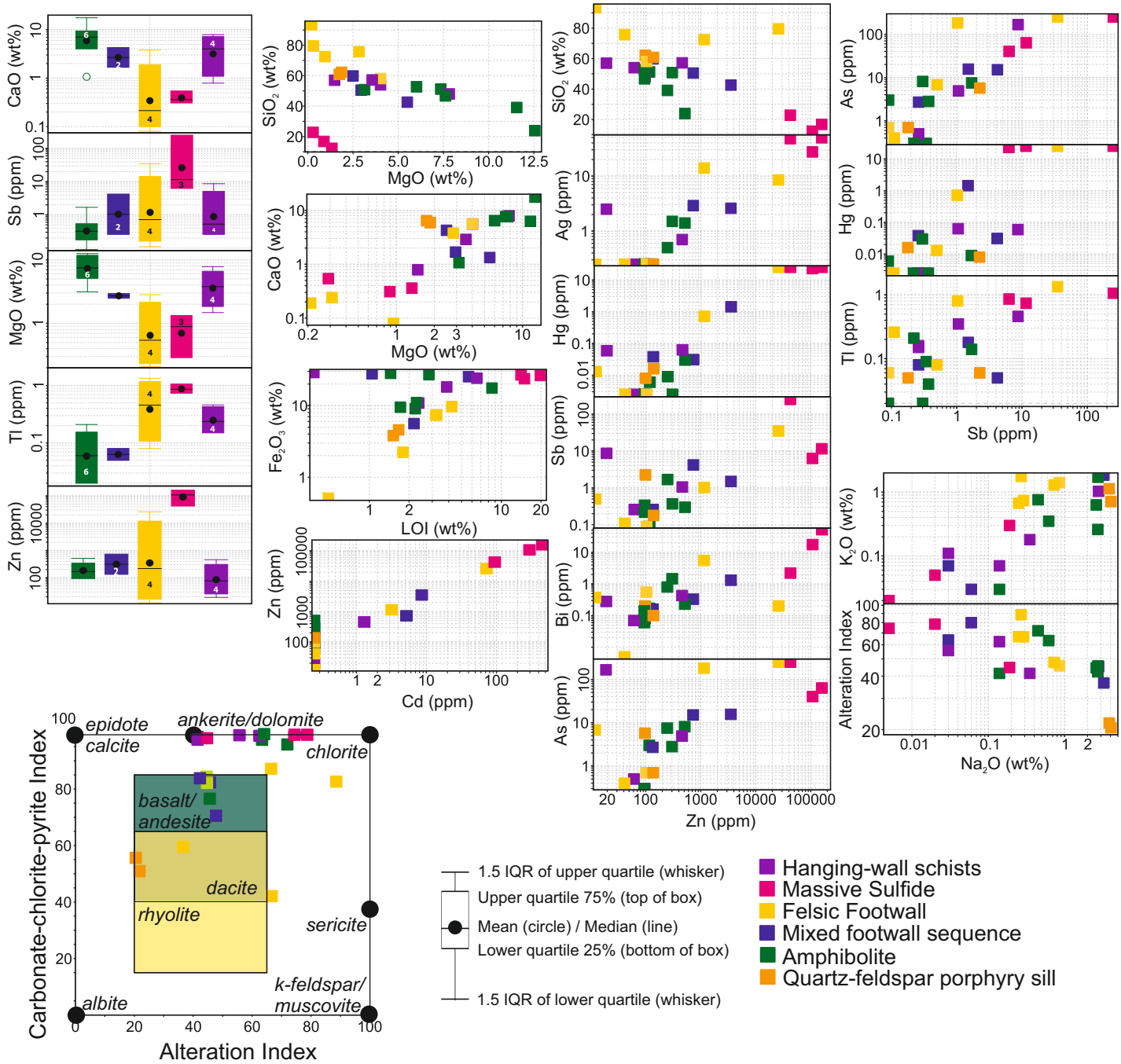




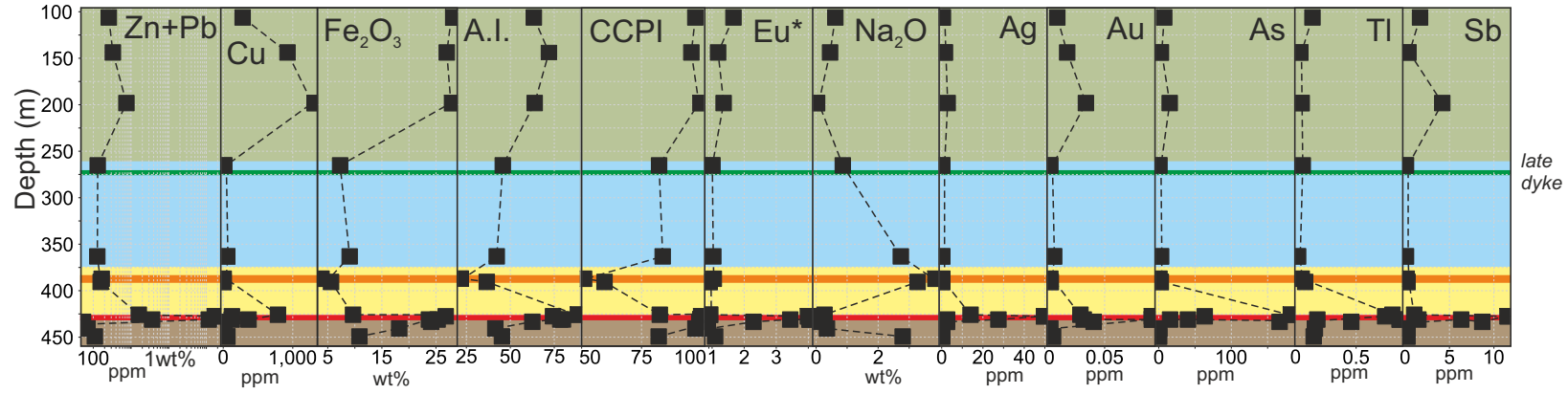




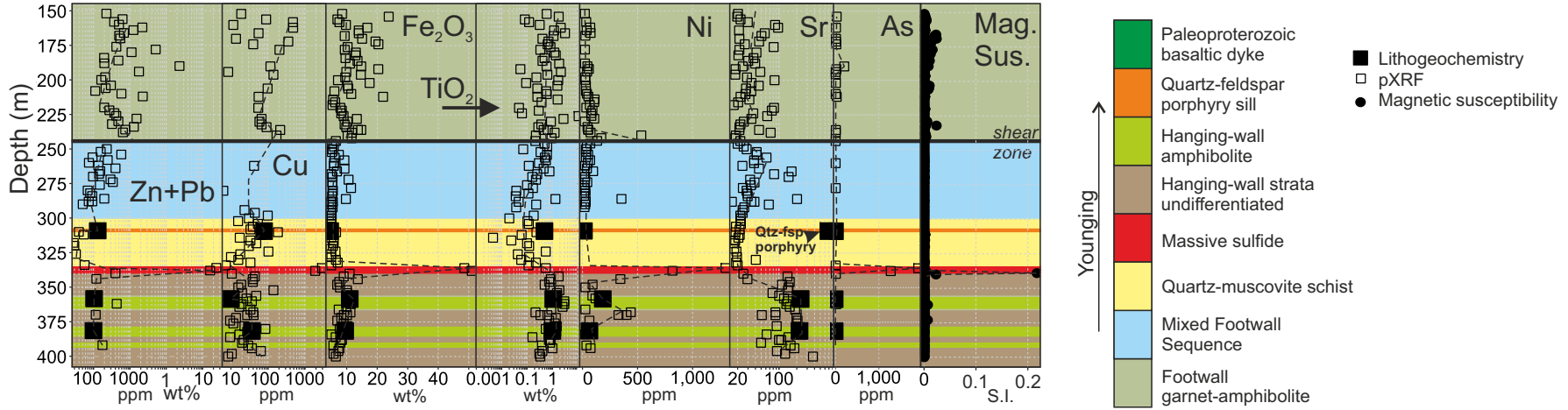




EC116D



EC056D



EC031D

